



The JWST-NIRCam View of Sagittarius C. I. Massive Star Formation and Protostellar Outflows

Downloaded from: <https://research.chalmers.se>, 2025-04-25 00:14 UTC

Citation for the original published paper (version of record):

Crowe, S., Fedriani, R., Tan, J. et al (2025). The JWST-NIRCam View of Sagittarius C. I. Massive Star Formation and Protostellar Outflows. *Astrophysical Journal*, 983(1).
<http://dx.doi.org/10.3847/1538-4357/ad8889>

N.B. When citing this work, cite the original published paper.



The JWST-NIRCam View of Sagittarius C. I. Massive Star Formation and Protostellar Outflows

Samuel Crowe¹ , Rubén Fedriani² , Jonathan C. Tan^{1,3} , Alva Kinman³ , Yichen Zhang⁴ , Morten Andersen⁵ ,
Lucía Bravo Ferres² , Francisco Nogueras-Lara⁵ , Rainer Schödel² , John Bally⁶ , Adam Ginsburg⁷ , Yu Cheng⁸ ,
Yao-Lun Yang⁹ , Sarah Kendrew¹⁰ , Chi-Yan Law¹¹ , Joseph Armstrong³ , and Zhi-Yun Li¹

¹ Department of Astronomy, University of Virginia, Charlottesville, VA 22904, USA; fec5fg@virginia.edu

² Instituto de Astrofísica de Andalucía, CSIC, Glorieta de la Astronomía s/n, E-18008 Granada, Spain

³ Department of Space, Earth & Environment, Chalmers University of Technology, 412 93 Gothenburg, Sweden

⁴ Department of Astronomy, Shanghai Jiao Tong University, 800 Dongchuan Rd., Minhang, Shanghai 200240, People's Republic of China

⁵ European Southern Observatory, Karl-Schwarzschild-Strasse 2, D-85748 Garching bei München, Germany

⁶ Center for Astrophysics and Space Astronomy, Astrophysical and Planetary Sciences Department, University of Colorado, UCB 389 Boulder, CO 80309, USA

⁷ Department of Astronomy, University of Florida, P.O. Box 112055, Gainesville, FL 32611, USA

⁸ National Astronomical Observatory of Japan, 2-21-1 Osawa, Mitaka, Tokyo 181-8588, Japan

⁹ Star and Planet Formation Laboratory, RIKEN Cluster for Pioneering Research, Wako, Saitama 351-0198, Japan

¹⁰ European Space Agency, Space Telescope Science Institute, Baltimore, MD 21218, USA

¹¹ Osservatorio Astrofisico di Arcetri, Largo Enrico Fermi, 5, 50125 Firenze FI, Italy

Received 2024 July 13; revised 2024 October 11; accepted 2024 October 16; published 2025 April 2

Abstract

We present James Webb Space Telescope (JWST) Near Infrared Camera observations of the massive star-forming molecular cloud Sagittarius C (Sgr C) in the Central Molecular Zone (CMZ). In conjunction with ancillary mid-IR and far-IR data, we characterize the two most massive protostars in Sgr C via spectral energy distribution (SED) fitting, estimating that they each have current masses of $m_* \sim 20 M_\odot$ and surrounding envelope masses of $\sim 100 M_\odot$. We report a census of lower-mass protostars in Sgr C via a search for infrared counterparts to millimeter continuum dust cores found with the Atacama Large Millimeter/submillimeter Array (ALMA). We identify 88 molecular hydrogen outflow knot candidates originating from outflows from protostars in Sgr C, the first such unambiguous detections in the infrared in the CMZ. About a quarter of these are associated with flows from the two massive protostars in Sgr C; these extend for over 1 pc and are associated with outflows detected in ALMA SiO line data. An additional ~ 40 features likely trace shocks in outflows powered by lower-mass protostars throughout the cloud. We report the discovery of a new star-forming region hosting two prominent bow shocks and several other line-emitting features driven by at least two protostars. We infer that one of these is forming a high-mass star given an SED-derived mass of $m_* \sim 9 M_\odot$ and associated massive ($\sim 90 M_\odot$) millimeter core and water maser. Finally, we identify a population of miscellaneous molecular hydrogen objects that do not appear to be associated with protostellar outflows.

Unified Astronomy Thesaurus concepts: Galactic center (565); Massive stars (732); Stellar jets (1607); Star formation (1569); H II regions (694); Stellar bow shocks (1586); Near infrared astronomy (1093); Millimeter astronomy (1061); Spectral energy distribution (2129)

Materials only available in the online version of record: figure sets

1. Introduction

Massive stars ($m_* > 8 M_\odot$) play a central role in star and planet formation, dispersing the natal clouds of their birth clusters and ionizing the interstellar medium through their radiation and winds. During the course of their stellar evolution, they drive much of the physical and chemical evolution of galaxies. The precise formation mechanism for massive stars, however, remains poorly understood, specifically whether they form in a similar, but scaled-up, manner as low-mass stars, i.e., core accretion models (e.g., C. F. McKee & J. C. Tan 2003), or whether they form more chaotically at the center of dense clusters, i.e., competitive accretion models (e.g., I. A. Bonnell et al. 2001; P. Wang et al. 2010;

M. Y. Grudić et al. 2022; see, e.g., J. C. Tan et al. 2014; A. L. Rosen et al. 2020, for reviews).

One of the most extreme star-forming environments in our Milky Way is the Central Molecular Zone (CMZ), which we define as the region within a Galactocentric radius of ~ 300 pc (see, e.g., J. D. Henshaw et al. 2023). This is a region of high metallicity (i.e., about $2 \times Z_\odot$; U. Gíveon et al. 2002; R. Schödel et al. 2020; M. Schultheis et al. 2021; F. Nogueras-Lara 2022), thermal pressures ($P_{\text{th}} \sim 10^{-10}$ erg cm $^{-3}$; M. Morris & E. Serabyn 1996), molecular gas temperatures (e.g., $\gtrsim 60$ K; A. Ginsburg et al. 2016), cosmic-ray ionization rates ($\zeta \gtrsim 10^{-15}$ s $^{-1}$; E. Carlson et al. 2016), and magnetic field strengths ($\gtrsim 50$ μ G over large scales and up to ~ 5 mG in dense molecular clouds; R. M. Crocker et al. 2010; T. Pillai et al. 2015). In addition, the CMZ region holds a large amount of molecular gas ($> 10^7 M_\odot$; K. Ferrière et al. 2007) but has a relatively low (by about an order of magnitude) star formation rate compared to empirical scaling relations derived from main disk regions; observational methods yield a current star formation rate of $\sim 0.08 M_\odot \text{ yr}^{-1}$ (J. D. Henshaw et al. 2023).

Table 1
Summary of the JWST/NIRCam Observations

Filter Pair (SW and LW)	Wavelength (μm)	Tracing Emission	Readout Pattern	Groups /Int	Integrations /Exp	Total Exp. Time (s)
F115W and F360M	1.15 and 3.60	cont.	SHALLOW2	3	1	773.047
F162M and F405N	1.62 and 4.05	H ₂ O and Br α	SHALLOW2	6	1	1739.357
F182M and F480M	1.82 and 4.80	H ₂ O and cont.	SHALLOW2	6	1	1739.357
F212N and F470N	2.12 and 4.69	H ₂	SHALLOW2	6	1	1739.357

Furthermore, there is an asymmetry of dense gas distribution (and therefore star formation) in the CMZ, with around 2/3 of the dense gas being located at positive (eastern) Galactic longitudes (F. Yusef-Zadeh et al. 2009; M. C. Sormani et al. 2018).

Sagittarius C (hereafter Sgr C) is an active star-forming region in the CMZ, and therefore one of the key laboratories for testing theories of star formation in this extreme environment (F. Yusef-Zadeh et al. 1984; C. Law & F. Yusef-Zadeh 2004; S. Kendrew et al. 2013; X. Lu et al. 2016, 2019a, 2019b, 2022). It is the most massive and luminous star-forming region in the western (negative longitude) side of the CMZ (S. Kendrew et al. 2013), and it has furthermore been suggested to be a connection point to a stream of gas and dust linking the CMZ and nuclear stellar disk to the Galactic bar (S. Molinari et al. 2011; J. D. Henshaw et al. 2023), potentially explaining the strong 24 μm emission in this region (S. J. Carey et al. 2009) as high amounts of warm dust heated by ionizing stars. This also explains the presence of large reserves of gas in this region that are necessary to produce the observed star formation activity.

Despite confusion surrounding the distance to the cloud due to its line-of-sight velocity, $\sim 60 \text{ km s}^{-1}$, which may imply a foreground distance of $\sim 5 \text{ kpc}$, previous studies have affirmed the cloud’s location at the CMZ distance based on its consistency with CMZ gas kinematics (S. Kendrew et al. 2013; J. M. D. Kruijssen et al. 2015; X. Lu et al. 2019b). Therefore, we adopt a distance to Sgr C as the general galactocentric distance measured by M. J. Reid et al. (2019) to be $8.15 \pm 0.15 \text{ kpc}$ based on water maser parallaxes.

Much attention has been paid to the most luminous source in the cloud, G359.44–0.102 (S. Kendrew et al. 2013), and its immediate surroundings. The source itself is a prominent “extended green object” (C. J. Cyganowski et al. 2008; X. Chen et al. 2013), a class of objects visualized in Spitzer IRAC images (identified in the 4.5 μm IRAC2 filter) and associated with massive star formation, methanol maser emission, and protostellar outflows. Accordingly, the source is associated with a Class II 6.7 GHz CH₃OH maser; additionally, a neighboring source is associated with both a CH₃OH maser (J. L. Caswell et al. 2010) and a 1665 MHz OH maser (W. D. Cotton & F. Yusef-Zadeh 2016), indicating that the region is forming at least two massive stars (S. L. Breen et al. 2013; X. Lu et al. 2019a). X. Lu et al. (2022) analyzed Atacama Large Millimeter/submillimeter Array (ALMA) Band 6 ($\sim 1.3 \text{ mm}$) observations of G359.44–0.102 to reveal that it is a massive protostar (measuring a stellar mass of $m_* \sim 30 M_\odot$) with a Keplerian disk with spiral features, potentially induced by dynamical interactions. The ALMA Band 6 molecular line data also indicate the presence of several protostellar outflows throughout the cloud, including a collimated jet proposed to have originated from G359.44–0.102 (see Figure 21 of X. Lu et al. 2021). S. Kendrew et al. (2013) also discuss the

possibility of an outflow from G359.44–0.102 on the basis of detection of faint atomic hydrogen (Br γ) and molecular hydrogen emission features in the region using infrared spectroscopy.

There has been some discussion about whether the rest of the Sgr C cloud is quiescent (e.g., S. Kendrew et al. 2013) or star-forming (e.g., X. Lu et al. 2016). From analysis of ALMA Band 6 continuum data, X. Lu et al. (2020) and A. V. I. Kinman et al. (2024) have found >100 low- to high-mass millimeter cores distributed throughout Sgr C, indicating that star formation is likely more widespread.

In this paper, we present JWST-Near Infrared Camera (NIRCam) observations of Sgr C, which provide an infrared view of its massive protostars, its lower-mass star-forming activity, and the wider environment surrounding the molecular cloud. Observations and reduction of the data used in this study are presented in Section 2. Our results are presented in Section 3. Discussion of the broader implications of these results is made in Section 4. A summary and conclusion are given in Section 5.

2. Observations and Data Reduction

2.1. James Webb Space Telescope

Observations with the James Webb Space Telescope (JWST) were taken on 2023 September 22 (Program ID 4147; PI: S. Crowe).¹² NIRCam (M. J. Rieke et al. 2005) was used with Primary Dither Type *FULLBOX* and Primary Dithers *6TIGHT*, i.e., a total of six dither positions. The final field of view (FOV) using this observing strategy is $\sim 2' \times 6'$. The filters used were paired in Short Wavelength (SW) and Long Wavelength (LW) filters, as listed in Table 1. Each SW filter has a pixel scale of $0''.031 \text{ pixel}^{-1}$, while each LW filter has a pixel scale of $0''.063 \text{ pixel}^{-1}$. The readout pattern for all filter pairs was *SHALLOW2* with Groups/Int 6 and Integrations/Exp 1 resulting in a total exposure time of 1739.357 s (except for the filter pair F115W and F360M, where Groups/Int 3 and Integrations/Exp 1 were used, resulting in a total exposure time of 773.047 s). The position angle with respect to the V3 axis (PA_V3) was $91^\circ.42$. See Table 1 for a summary of the observations.

The data were reduced using the Python package JWST pipeline (version = 1.12.5; H. Bushouse et al. 2023) and the Calibration Reference Data System Context = `jwst_1217.pmap`. The raw data, i.e., the UNCAL frames, were downloaded from the MAST archive using the Python package `astroquery` (A. Ginsburg et al. 2019; C. E. Brasseur et al. 2020).

¹² The JWST data presented in this article were obtained from the Mikulski Archive for Space Telescopes (MAST) at the Space Telescope Science Institute. The specific observations analyzed can be accessed via doi:10.17909/p8dv-8593.

We then ran the standard JWST reduction in the three stages, but modifying a number of default parameters, which we summarize below:

1. *Stage 1.* This involves applying the basic detector-level corrections to our imaging uncalibrated mutilaccum ramp products. We set the `suppress_one_group=False` in the input `ramp_fit` to recover saturated pixels between the first and second read. The rest was set as default.
2. *Stage 2.* This involves applying instrumental corrections and calibrations to the output products from Stage 1. All input parameters were set to the default values.
3. *1/f noise removal.* $1/f$ noise is a pixel-to-pixel correlated noise, causing horizontal banding in JWST NIRC*am* images. The distinctive pattern of $1/f$ noise varies with each readout of the detector. Despite the ramp-fitting step in the pipeline (Stage 1) reducing this noise, traces of it remain visible in the resulting rate images. This effect is not removed in the standard JWST reduction. We used the script `image_loverf.py`.¹³ The tool is designed to run on the calibrated files that are output from the Stage 2 pipeline. In summary, the script subtracts a background and masks sources to determine $1/f$ stripes. The input parameters used were `sigma_bgmask=3.0`, `sigma_1fmask=2.0`, `splitamps=True`, and `usesegmask=True`. The former input assumes that these stripes can be split, whereas the latter input allows us to use a segmentation image as the mask before fitting the $1/f$ stripes. The output from this script can be used through the Stage 3 pipeline as usual. We only applied this correction to the SW filters, i.e., F115W, F162M, F182M, and F212N, which improved the image quality significantly. On the other hand, the LW filters showed no improvement, or even a slight decrease in the image quality, when the $1/f$ noise removal was applied. Therefore, we used the LW images without applying this correction.
4. *Stage 3.* This involves taking the calibrated slope images and combining them into the final mosaics. The `pmap` version used provided us with accurately aligned mosaics between modules A and B. Here we also forced the final shape of the image (i.e., the number of pixels in the x - and y -axes) to be the same between filters. We set a final shape for the LW of 5660×2280 and the SW filters of $11,450 \times 4740$. To do this, we set, in the `resample` step, the argument `output_shape: (2280, 5660)` for the LW filters and `output_shape: (4740, 11450)` for the SW filters. This facilitated the registration between filters. We also set celestial north up and east to the left, aligning with the pixel axes y and x , respectively, by setting in the `resample` step the argument `rotation: 0.0`.
5. *Registration.* The output images, after the three stages of reduction, were aligned in the World Coordinate System to the Gaia DR3 reference frame (Gaia Collaboration et al. 2023). However, in the pixel frame, there were subpixel shifts between the images. Therefore, we registered the images to the F470N and F212N filters for the LW and SW filters, respectively. We did this using the Python package `astroalign` (M. Beroiz et al.

2020). To do this, we applied an affine transformation using common stars in the images.

2.1.1. Continuum-subtracted Images

To characterize the line-emitting structures in the narrow-band images, particularly shocked emission from protostellar outflows, continuum-subtracted images were made following the methods detailed in K. S. Long et al. (2020) and used in S. Crowe et al. (2024). Briefly, the method involves sampling the flux from ~ 15 to 20 isolated, nonsaturated point sources throughout a given region in both continuum- and narrowband images in order to constrain the ratio between their fluxes, which is used to scale the continuum data to subtract from the narrowband images pixel by pixel. Although the NIRC*am* images are already normalized for the differences in bandwidth of each filter (having units of MJy sr^{-1}) and could be subtracted directly, the former method is effective at accounting for differences between the continuum and line image fluxes owing to the high levels of extinction in this region, which F. Nogueras-Lara (2024) has shown to be $\sim 2.6 A_K$, on the basis of red giant color analysis (see F. Nogueras-Lara et al. 2022, for a description of the methods).

Due to the large size of the images ($2' \times 6'$), we split each image into four main parts for the creation of continuum-subtracted images using the above method: one part containing the Sgr C protocluster and extended molecular cloud, a second part enclosing the star-forming region G359.42–0.104 (see Section 3.5) and the western-most side of the image, a third part enclosing the rest of the southern half of the image (i.e., most of the bright H II region), and a fourth part that covers the rest of the northern half of the image (see Figure 1). We note that the flux ratio between the line and continuum images varied by $<10\%$ over all parts of the image.

The above method was carried out directly for the F470N image, from which we subtracted the F480M image. We acknowledge the caveat that, given the overlap between the filters, there will inevitably be some H₂ 4.7 μm line emission in F480M that is inadvertently subtracted from the F470N image; however, given that the bandpass of F480M is relatively large compared to that of F470N (0.303 μm for F480M compared to 0.051 μm for F470N; i.e., $6\times$ higher bandpass¹⁴), this subtle “oversubtraction” poses negligible impact to the fluxes in the F470N continuum-subtracted images, meaning that at most 1/6 of the H₂ flux is over subtracted in the F470N image. The same general method was used to subtract the F212N image using the F182M image.

The F405N image was subtracted by linearly interpolating the F360M and F480M image fluxes at each pixel to estimate the continuum flux at 4.05 μm . This interpolation is considered more robust than taking flux from a single filter, since F360M and F480M provide an estimate of the continuum emission on both the blue and red sides of F405N without themselves being contaminated with any Br α flux. Similar methods have been adopted for continuum subtraction of the F335M filter to isolate polycyclic aromatic hydrocarbon (PAH) emission in nearby star-forming galaxies (see, e.g., Section 3.1 of B. Gregg et al. 2024).

We note that the continuum subtraction performed imperfectly on some of the stars in the image, producing residuals as

¹³ https://github.com/chriswillott/jwst/blob/master/image_loverf.py

¹⁴ <https://jwst-docs.stsci.edu/jwst-near-infrared-camera/nircam-instrumentation/nircam-filters>

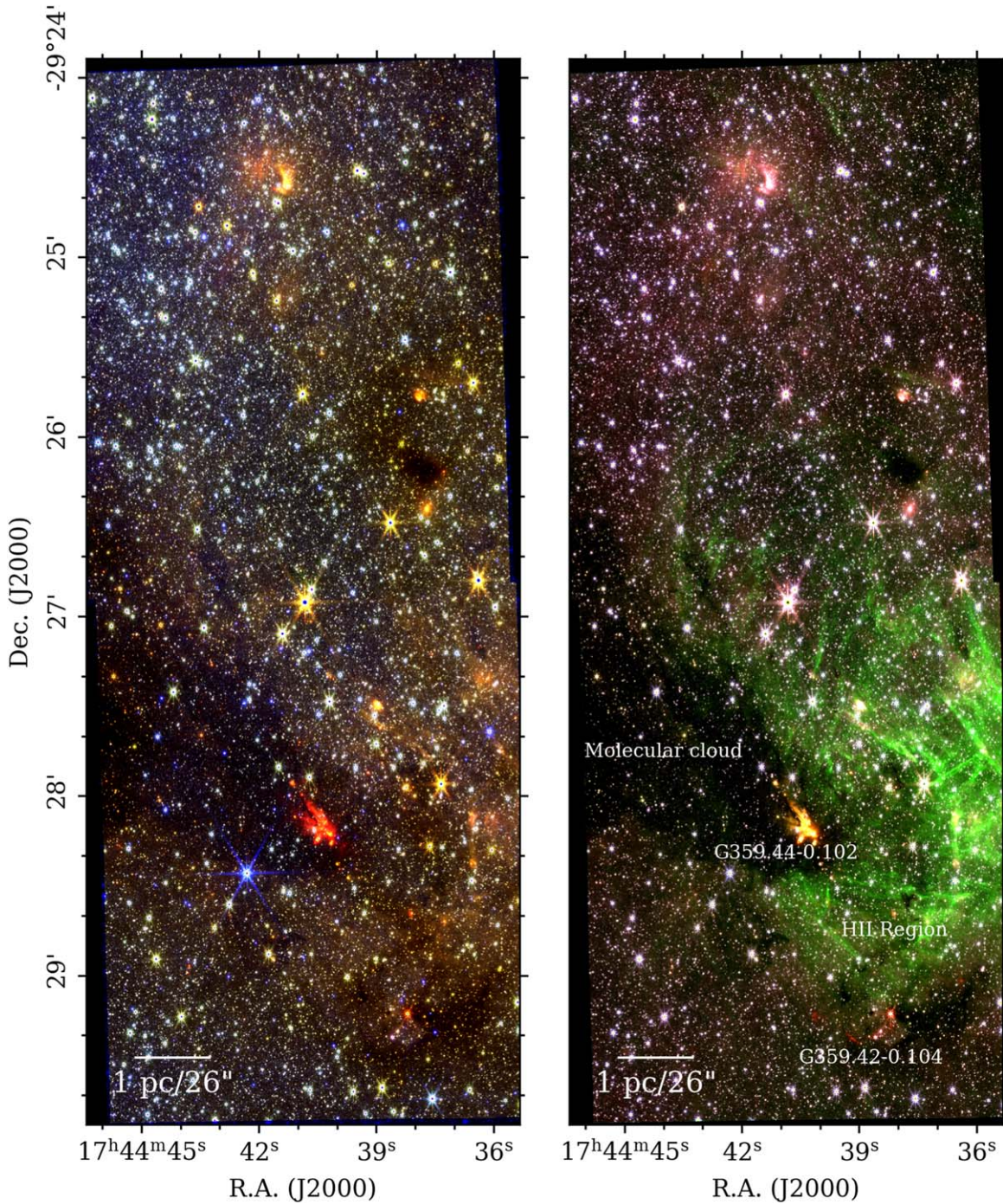


Figure 1. RGB image of Sgr C showing two different color schemes. North is up and east is to the left in both panels. Left: “continuum” image with F480M shown in red, F360M in green, and F182M in blue. Right: “emission-line” image with F470N shown in red, F405N in green, and F360M in blue. Notable features discussed in the text are labeled.

a combination of dark and bright pixels. These are mainly due to the fact that the stellar point-spread functions (PSFs) between NIRCcam filters are diffraction limited and therefore wavelength dependent. We also note imperfections in some regions of nebulosity in the image resulting from color differences in these regions with respect to the stars. These features are typical in continuum-subtracted images (e.g., M. Reiter et al. 2022; J. Bally & B. Reipurth 2023) and do not have any significant effect on our characterization of the authentic features in the images.

2.2. Archival Data

The mosaicked 25 and 37 μm images provided by the Stratospheric Observatory for Infrared Astronomy (SOFIA) FORCAST Galactic Center Legacy Survey (SOFIA Level 4 data products; M. J. Hankins et al. 2020) were used to provide mid-infrared (MIR) and far-infrared (FIR) fluxes for spectral energy distribution (SED) fitting. Note that the survey covers a total area of 403 arcmin² (2180 pc²), including regions such as the Sgr A, B, and C complexes and the 50 km s⁻¹ molecular cloud. However, in this paper we limit our analysis to the

region observed with JWST, Sgr C. In addition, archival images from the Spitzer Space Telescope GALCEN survey (S. Stolovy et al. 2006) at 3.6, 4.5, 5.6, and 8.0 μm and from the Herschel infrared Galactic Plane Survey (Hi-GAL; S. Molinari et al. 2016) at 70, 160, 250, 350, and 500 μm were used for SED fitting.

2.3. Atacama Large Millimeter/Submillimeter Array

We used ALMA Band 6 (1.3 mm) continuum and spectral line data (Program ID 2016.1.00243.S) in Sgr C (X. Lu et al. 2020) to compare to our JWST data. The synthesized beam size of these observations is $0''.25 \times 0''.17$, and the rms noise is in the range 40–60 $\mu\text{Jy beam}^{-1}$.

We also utilized ALMA Band 3 (3 mm) continuum data from the ALMA Central Molecular Zone Exploration Survey (ACES) program (Program ID 2021.1.00172.L; PI: Longmore). The beam size of these observations is $1''.97 \times 1''.52$, and the rms noise is ~ 0.2 mJy beam $^{-1}$. We use the Band 3 data solely to explore the region G359.42–0.104 (see Section 3.5). A full description of the reduction of this data will be given in A. Ginsburg et al. (2024, in preparation), D. Walker et al. (2024, in preparation), and S. Longmore et al. (2024, in preparation); however, some additional details about the survey and data reduction can be found in A. Ginsburg et al. (2024) and M. Nonhebel et al. (2024).

3. Results

Here we present the near-infrared (NIR) data obtained from JWST NIRCам on the Sgr C molecular cloud, featuring broad and deep coverage of the entire cloud, its associated H II region, and the surrounding environment. We use this imaging to directly characterize three luminous massive protostars via SED fitting, identify as young stellar object (YSO) candidates five highly reddened IR sources that have matching ALMA Band 6 dust cores, and survey 88 bright line emission features, most likely knots of shocked outflow emission produced by over a dozen protostellar outflows. Some of the star formation activity is located in a newly discovered region, $\sim 1'$ to the south of Sgr C.

3.1. Overview of NIRCам Imaging of the Sgr C Region

The left panel of Figure 1 shows an RGB image of Sgr C and its surroundings, covering a total FOV of $2' \times 6'$. Red is used for F480M, green for F360M, and blue for F182M emission. We expect that these filters mainly trace continuum emission, especially from stars. Glowing red in the lower middle of the image is the primary target of the observation, the massive protostellar source G359.44–0.102 in Sgr C, and its associated protocluster. This source is surrounded by a relatively dark region, which is inferred to be a dusty molecular cloud, which blocks much of the light from background stars. This cloud extends mainly to the east and north of the protocluster. Other dark clouds are also apparent in the image, including prominent examples at R.A. $\sim 17^{\text{h}}44^{\text{m}}37^{\text{s}}$, decl. $\sim -29^{\circ}26'10''$, to the NW of G359.44–0.102 and at R.A. $\sim 17^{\text{h}}44^{\text{m}}38^{\text{s}}$, decl. $\sim -29^{\circ}29'30''$, which we will see is associated with the star-forming region G359.42–0.104 (see Section 3.5).

The right panel of Figure 1 shows the same region, but now red is used for the F470N filter (covering the H₂ 0–0 S(9) line at 4.6947 μm), green for F405N (covering the H I line Br α at 4.05 μm), and blue for F360M, which mostly covers continuum

emission at 3.6 μm . Most prominent in this image is the glow of hydrogen recombination line emission Br α , which traces ionized gas surrounding G359.44–0.102 in northern, western, and southern directions. We note that the lack of Br α emission to the east could potentially be explained by extinction of the main Sgr C dark cloud, i.e., an infrared dark cloud. The Br α nebula displays remarkable linear, “needle”-like features, which have a variety of orientations. We discuss this Br α emission further in Section 4, while its main analysis will be presented in a forthcoming paper.

Also present in the right panel of Figure 1 are “knots” of emission that appear red and trace H₂ 0–0 S(9) line emission, i.e., excited molecular hydrogen, that may be powered by shocks from protostellar outflows. These are key tracers of star formation activity, which we discuss extensively in Section 3.4.

3.2. The Massive Protostars in Sgr C

There are two main massive protostars in Sgr C, which we refer to as G359.44a (G359.44–0.102; see Section 1) and G359.44b. Figure 2 shows the inner region surrounding both protostars in several NIRCам filters, all of which trace predominantly continuum emission from the protostars, including scattered light in their outflow cones. The protostar G359.44a itself can be seen in F480M (top left panel of Figure 2), along with its outflow cone, which extends in “green” emission toward the northeast part of the image. A bright limb of the inner cone near G359.44a (marked with a white plus sign) can be seen in bright “red” emission. Nebulosity associated with the outflow axis of G359.44b can also be seen in “green” to the east, although the protostar itself is not a prominent infrared source. Going to shorter wavelengths, the emission from both protostars drops off dramatically, likely due to the effects of high extinction toward the heart of the protocluster and toward Sgr C in general ($\sim 2.6 A_K$; F. Noguera-Lara 2024). In F360M, G359.44a still appears to be visible as a point source, and extended continuum emission is seen tracing its outflow cone; additionally, some emission can be seen in F182M toward the northeast of G359.44a and toward the northwest of G359.44b, likely reflected light off of the outflow cavity walls very close to each protostar. Both protostars and their associated outflows are, however, essentially invisible in both F162M and F115W.

SED fitting was performed on these two massive protostars to place constraints on their physical properties. We note that these sources are collocated with millimeter continuum cores sgrc65 and sgrc22, respectively, that were identified by X. Lu et al. (2020). The central coordinates of G359.44a and G359.44b are (R.A. = $17^{\text{h}}44^{\text{m}}40^{\text{s}}23$, decl. = $-29^{\circ}28'14''.903$) and (R.A. = $17^{\text{h}}44^{\text{m}}40^{\text{s}}63$, decl. = $-29^{\circ}28'15''.458$), respectively, with these positions defined from the local emission peaks of the SOFIA-FORCAST 37 μm image.

The SEDs were constructed using JWST NIRCам 1.62, 1.82, 3.60, and 4.80 μm ; Spitzer IRAC 3.6, 4.5, 5.6, and 8.0 μm ; SOFIA-FORCAST 25 and 37 μm ; and Herschel PACS and SPIRE 70, 160, 250, 350, and 500 μm data (see Section 2). Aperture photometry and SED construction were performed using the open-source Python package *sedcreator* (R. Fedriani et al. 2023b), generally following methods developed in the SOFIA Massive (SOMA) Star Formation Survey (J. M. De Buizer et al. 2017; M. Liu et al. 2019, 2020; R. Fedriani et al. 2023b). However, the Sgr C massive protostars are relatively closely separated, i.e., by $\sim 5''$. This is smaller than the

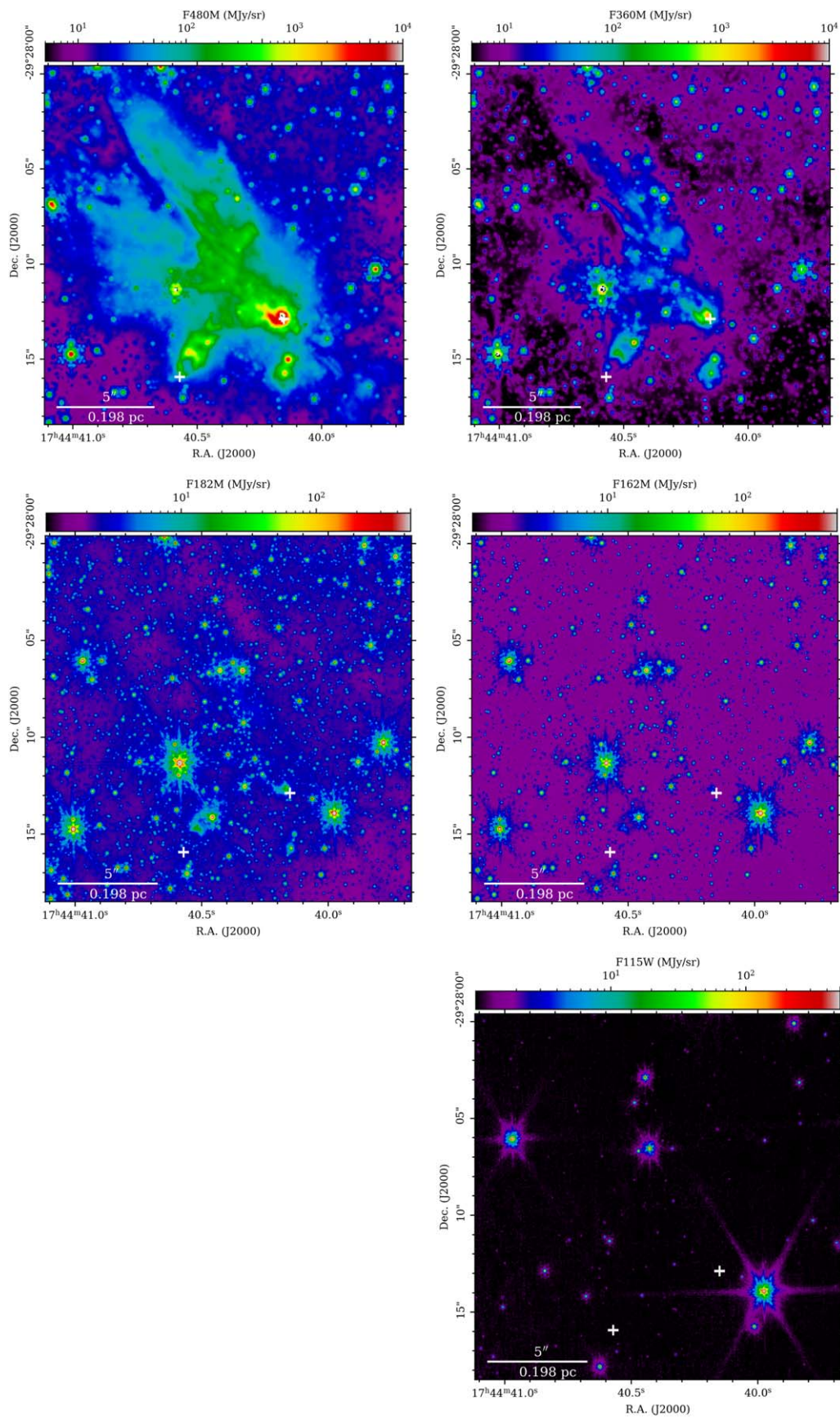


Figure 2. Five-panel view of the heart of the Sgr C protocluster in several NIRCcam filters, shown and labeled in descending order of wavelength from left to right, top to bottom. North is up and east is to the left in all panels. Indicated as white plus signs are the massive protostars G359.44a (western marker) and G359.44b (eastern marker; see text). Coordinates for each protostar are taken from X. Lu et al. (2020). A logarithmic scale is used to highlight both the bright emission features (e.g., the outflow cone surrounding G359.44a) and the dimmer nebulosity and sources surrounding the massive protostars.

minimum separation normally treated in the SOMA Survey of $10''$, which allows each source to have a minimum aperture radius of $5''$ (the resolution of Herschel at $70 \mu\text{m}$). Thus, rather than the standard SOMA method of using the Herschel $70 \mu\text{m}$ image to define source apertures, we define these from the longest-wavelength image at which they are clearly resolved, i.e., SOFIA-FORCAST $37 \mu\text{m}$. The aperture radii are derived using the automated algorithm of R. Fedriani et al. (2023b) applied to this image, in which the aperture size is increased from a minimum size of $3''$ until background-subtracted flux attains an approximate plateau, with the background evaluated in an annulus from one to two aperture radii, excluding overlap with nearby source apertures (Z. Telkamp et al. 2024, in preparation). The fitted aperture radii for the two sources are $4''.25$. Pixels overlapping both apertures are distributed to the closer source. These aperture geometries are held fixed for evaluating the fluxes at wavelengths of $37 \mu\text{m}$ and shorter.

For longer wavelengths, where the sources are unresolved, we use the same algorithm to define a new joint aperture for the two sources, based on the $70 \mu\text{m}$ image, of $9''$, centered in the $70 \mu\text{m}$ emission peak via visual inspection at (R.A. = $17^{\text{h}}44^{\text{m}}40^{\text{s}}19$, decl. = $-29^{\circ}28'15''.344$). We then distribute the fluxes and errors to G359.44a and G359.44b in a 3:1 ratio for all wavelengths $\geq 70 \mu\text{m}$, based on the flux ratio of the sources in the $37 \mu\text{m}$ image (the longest-wavelength image in which the sources are still resolved). This approximation appears to be valid in the $70 \mu\text{m}$ image, where G359.44a appears to remain the brighter source.

Photometry was conducted in all filters with the above apertures, and errors are assigned for each flux; for fluxes below $100 \mu\text{m}$ this error is derived from fluctuations in the background flux taken from the annulus (see R. Fedriani et al. 2023b), and for fluxes above $100 \mu\text{m}$ this error is taken as the integrated background flux over the annulus (from one to two aperture radii). All errors are taken in quadrature with an assumed systematic error of 10%. All fluxes and their associated error for each wavelength for each source are given in Appendix A.

The observed SEDs were then fit to the model grid of radiative transfer models of massive star formation via monolithic core collapse from Y. Zhang & J. C. Tan (2018), which has primary parameters of mass surface density of the clump environment Σ_{cl} , initial core mass M_c , current stellar mass m_* (which measures the extent of evolution of a given protostellar model), inclination angle θ_{view} , and level of foreground extinction A_V . The goodness of fit of models was then assessed via a reduced χ^2 parameter, and since SED fitting results are subject to degeneracies (e.g., between A_V and θ_{view} , and between Σ_{cl} and θ_{view} ; see Y. Zhang & J. C. Tan 2018, for more information), we present averages of the results of “good” model fits, following the methods of R. Fedriani et al. (2023b), which we describe here. If the minimum χ^2 of all models in the fitting routine, χ_{min}^2 , is less than 1, we average together all models with $\chi^2 < 2$; if $\chi_{\text{min}}^2 > 1$, we average all models with $\chi^2 < 2 \times \chi_{\text{min}}^2$. We note that, following methods from J. M. De Buizer et al. (2017), M. Liu et al. (2019, 2020), and R. Fedriani et al. (2023b), all fluxes below $10 \mu\text{m}$ were designated as upper limits owing to the addition of strong contaminants to the emission at these wavelengths (e.g., from PAH bands) that are not modeled by the Y. Zhang & J. C. Tan (2018) model grid. We also note that we exclude models that

predict a core size that is greater than twice the aperture used to define the SED, i.e., $R_c > 2 \times R_{\text{ap}}$.

G359.44a, G359.44b, their SEDs, and the 2D parameter space plots of their fitting are shown in Figure 3. A summary of key physical parameters from the fitting results is given in Table 2. Note that this table contains fitting results for an additional massive protostar candidate, G359.42a, which is outside the main Sgr C cloud and will be discussed in Section 3.5.

We note a good agreement in the SED for each protostar between the Spitzer and NIRCcam data points (see the data points below $10 \mu\text{m}$ in their SEDs), and we note that the additional NIRCcam points do not appear to have significantly altered the results of the fitting. A peak in each SED at $70 \mu\text{m}$ is also seen, as is typical of the SEDs of massive protostars (see, e.g., R. Fedriani et al. 2023b).

3.3. A Search for Low-mass Protostars

To search for lower-mass protostars in the Sgr C region, we start with the 1.3 mm emission cores detected by ALMA. We ran a dendrogram source-finding algorithm (E. W. Rosolowsky et al. 2008) using the following parameters: minimum flux density of 4σ , minimum significance of a structure of 1σ , and minimum area of a structure of one beam. These values were adopted to match those used by X. Lu et al. (2020), and we verify that we recover the same sources as presented in their study. Of the 274 cores in X. Lu et al. (2020), 267 are within the FOV of the NIRCcam observations.

We next used the *Starfinder* tool to extract PSFs and perform photo-astrometry on the NIRCcam filters F162M, F360M, and F480M (E. Diolaiti et al. 2000). In brief, we constructed the PSFs for each mosaic by selecting bright, unsaturated, isolated stars, running source detection and iterating on the procedure. The cores of all but the most strongly saturated stars were repaired via PSF fitting. Finally, we performed photo-astrometry with a 5σ threshold (using the error maps provided by NIRCcam as noise). This algorithm was run on a $150'' \times 90''$ box centered at the coordinates (R.A. = $17^{\text{h}}44^{\text{m}}42^{\text{s}}85$, decl. = $-29^{\circ}27'20''.055$), enclosing the entire part of the Sgr C cloud covered by the NIRCcam data, resulting in the identification of 91,642 sources in F162M, 40,287 sources in F360M, and 40,382 sources in F480M. We refer further details to a follow-up paper focused on the global stellar population in the NIRCcam images.

Cross-matching between IR sources and ALMA cores was carried out for those sources identified in the longest NIRCcam wavelength of $4.8 \mu\text{m}$ (F480M), where we expect embedded protostars to be relatively bright and dust extinction to be minimized. A source was considered to match an ALMA core if its position was within $0''.10$, i.e., half an ALMA beam, from the peak of the dust emission. This corresponds to a physical projected separation of about 800 au. Using this criterion, 23 of the ALMA cores were found to have a matching F480M source.

Due to the high stellar density of the CMZ, there is a possibility that some of these 23 mm/NIR matches are aligned by chance. We estimate the expected number of spurious matches in the following way. First, we calculate the stellar density of the field by dividing the number of F480M sources in the *Starfinder* catalog by the area of the field. The source density is 3.0 sources arcsec^{-2} , or $\lambda = 0.10$ sources per FWHM ALMA beam. If we assume that the number of sources in a

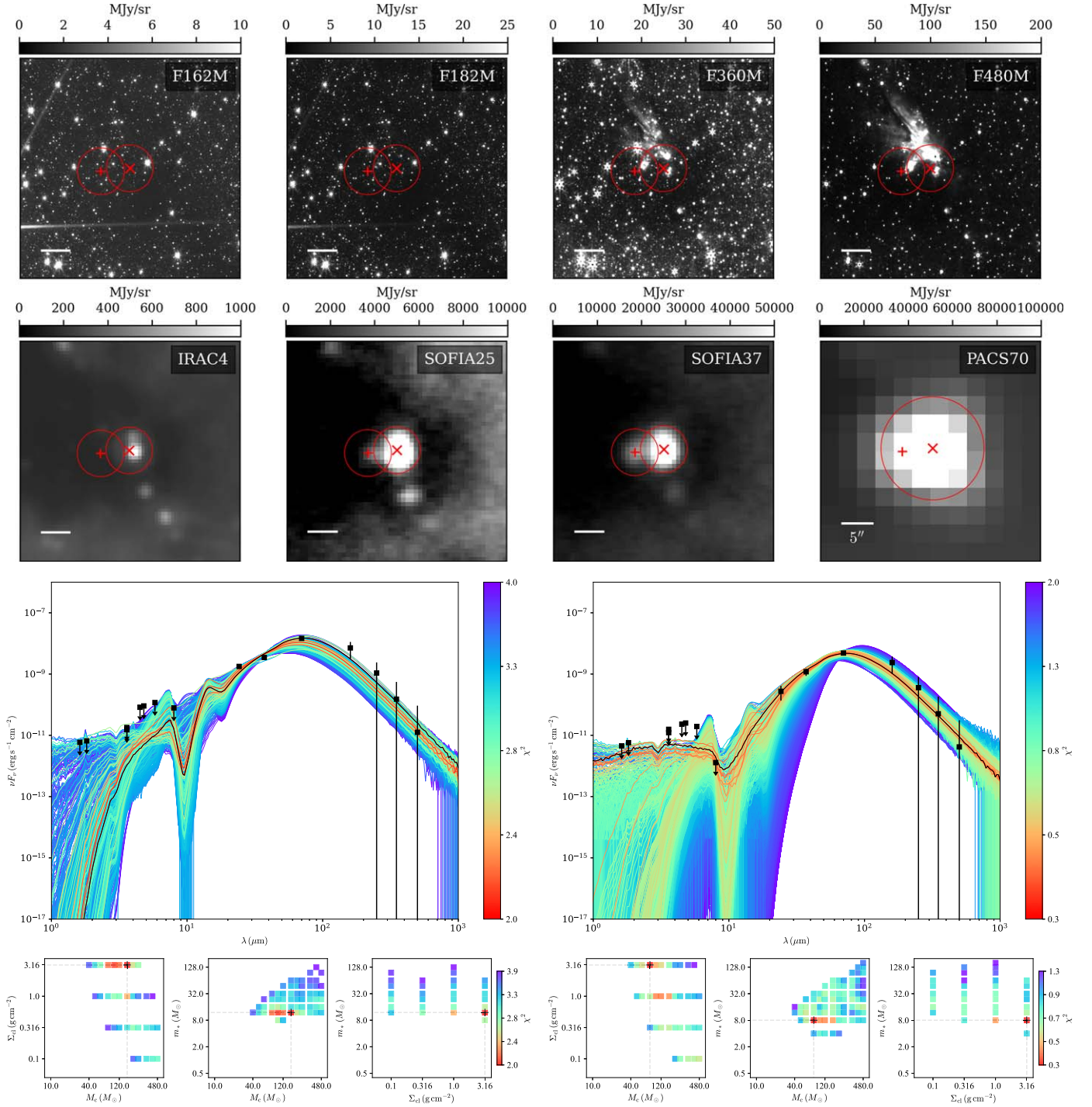


Figure 3. Top: eight-panel image of the protostars G359.44a (red cross) and G359.44b (red plus sign) in NIR and MIR filters. Note that the plotted coordinates of each protostar have been chosen from their peak emission in the SOFIA 37 μ m image and are therefore different from the coordinates shown in Figure 2. A physical bar of 5'' is shown in the lower left corner of each panel. The aperture(s) used for photometry at each wavelength, as discussed in the text, are shown. Middle: protostellar SED for G359.44a (left) and G359.44b (right), with model fittings overlaid and color-coded by χ^2 , with the best-fit SED as a black line. Bottom: 2D parameter space plots from the SED fitting results for G359.44a (left) and G359.44b (right). Various parameter pairings are given on the x- and y-axes of each plot, with each pairing of parameter values color-coded by χ^2 . Dashed gray lines indicate the lowest χ^2 (i.e., best-fitting) pair of parameter values.

given ALMA beam follows a Poisson distribution, we can calculate the probability that an ALMA beam (i.e., the area within matching distance of a core peak) contains at least one source by chance. The probability is $1 - P(0 \text{ sources in beam}) = 1 - e^{-\lambda} = 0.095$. This means that we expect ~ 25 cores to have NIR matches by chance. The detected number of matches, 23, is almost identical. Therefore, we cannot

rely on spatial coincidence alone to find YSOs but need to use an additional metric, reddening, to identify YSO candidates.

Therefore, the 23 identified F480M sources were matched to sources in the filters F360M and F162M in order to investigate their reddening. Reddening could give an indication of whether the source is likely to be a foreground star or is at the galactocentric distance (F. Noguera-Lara et al. 2021), and

Table 2
SED Fitting Results, Averaged over All “Good” Model Fits (See Text), for Massive Protostars in Sgr C and G359.42–0.104

Name	M_c (M_\odot)	Σ_{cl} (g cm^{-2})	m_* (M_\odot)	θ_{view} (deg)	M_{env} (M_\odot)	L_{bol} (L_\odot)	M_{disk} (M_\odot)	\dot{M} ($M_\odot \text{ yr}^{-1}$)	Age (yr)	A_V (mag)
G359.44a	$188.5^{+165.5}_{-88.1}$	$0.46^{+1.14}_{-0.33}$	$20.7^{+14.1}_{-8.4}$	63 ± 17	$119.6^{+168.7}_{-70.0}$	$9.7^{+15.6}_{-6.0} \times 10^4$	$6.9^{+4.7}_{-2.8}$	$3.0^{+3.7}_{-1.6} \times 10^{-4}$	$1.2^{+1.6}_{-0.7} \times 10^5$	91 ± 69
G359.44b	$202.9^{+179.0}_{-95.1}$	$0.72^{+1.60}_{-0.50}$	$20.4^{+24.1}_{-11.0}$	60 ± 20	$132.3^{+159.1}_{-72.2}$	$1.0^{+3.1}_{-0.8} \times 10^5$	$6.8^{+8.0}_{-3.7}$	$4.2^{+5.0}_{-2.2} \times 10^{-4}$	$8.6^{+13.9}_{-5.3} \times 10^4$	423 ± 296
G359.42a	$32.9^{+40.7}_{-18.2}$	$0.26^{+0.50}_{-0.17}$	$8.5^{+11.9}_{-5.0}$	49 ± 25	$5.4^{+9.3}_{-3.4}$	$8.2^{+41.7}_{-6.9} \times 10^3$	$2.8^{+4.0}_{-1.7}$	$4.3^{+3.9}_{-2.1} \times 10^{-5}$	$2.1^{+3.0}_{-1.2} \times 10^5$	35 ± 25

additionally whether it is an ordinary star in the CMZ or may be an embedded (highly reddened) YSO.

First, the small offsets between the coordinates of F162M, F360M, and F480M were compensated for by subtracting the median x and y separation between F162M/F360M source positions and source positions in F480M (-0.5483 LW pixels in x , -0.6718 LW pixels in y for F162M; $+0.0340$ LW pixels in x , -0.7740 LW pixels in y for F360M). The median separation was obtained by a preliminary cross-matching to 1000 randomly selected sources in the F480M source catalog. After offset correction, sources in the F360M and F162M filters were cross-matched to the F480M sources with matching ALMA cores. If the distance between positions was less than one long-wavelength pixel, i.e., $0''.063$, the sources were considered to be matching. Out of the 23 F480M sources with ALMA counterparts, this resulted in 13 matches with F360M and 14 matches with F162M.

The magnitude of the sources was calculated in all three filters, as well as the color index F162M – F480M. In the case where a source was undetected at the shorter wavelength, the completeness limit of the source catalog ($m_{\text{F162M}} = 23.2$, dominated by crowding) was used to obtain a lower limit on the color index. A list of all ALMA cores with matching F480M sources is shown in Table 3. The sources are listed in order of increasing distance between the ALMA peak and the F480M source.

To determine which sources were significantly reddened, their color indices were compared to the mean and standard deviation of the color index in the full F480M source catalog. A color–magnitude diagram of all F480M sources with an F162M counterpart can be seen in Figure 4. By similar analysis to that of F. Noguera-Lara (2024), we apply a color cut of ~ 3.2 to separate foreground stars from stars in the CMZ. Excluding the foreground stars, the mean color index of these sources was 4.54, and the standard deviation was 0.81. Five of the ALMA-matching sources have a reddening more than two standard deviations above the mean. These are taken to be our sample of strong YSO candidates. Out of these five sources, only one (sgrc41) is detected in all bands (F162M, F360M, F480M). We note that all five of these sources have associated millimeter core masses between ~ 1 and $2 M_\odot$ (see Table 3), implying that they may be low-mass YSOs, although it must be noted that these masses do not represent the masses of the YSOs themselves. Additionally, none of these five sources are visible in the MIR/FIR emission (e.g., from SOFIA, Herschel), which implies that they are much dimmer than the massive protostars in the cloud, G359.44a and G359.44b, so as to be below the sensitivity limit of those observations. This would also imply that these are low-mass rather than high-mass protostar candidates.

Figure 5 shows all 23 ALMA cores that have a matching F480M source. Red dendrogram contours and millimeter peaks are overlaid on the F162M, F360M, and F480M NIRC

Cam images. The matching NIR source detected in the respective images is marked with a cyan plus sign. Figure 6(b) also shows the spatial locations of these sources in the Sgr C cloud.

3.4. Outflow Knot and Outflow Source Identification

Protostellar outflow features were identified in F212N, F405N, and F470N continuum-subtracted images (Section 2.1.1). F212N and F470N trace two bright shock-excited H_2 lines ($\nu = 1-0 \text{ S}(1)$, $\lambda = 2.1218 \mu\text{m}$ for the former and $\nu = 0-0 \text{ S}(9)$, $\lambda = 4.6947 \mu\text{m}$ for the latter), generally associated with shocked material from both collimated jets and wide-angle outflows from protostars (see, e.g., T. P. Ray et al. 2023). F405N traces atomic hydrogen recombination emission, particularly the $\text{Br}\alpha$ ($n = 5-4$; $\lambda = 4.05 \mu\text{m}$) line. $\text{Br}\alpha$ and $\text{Br}\gamma$, another line in the Brackett series at $\lambda = 2.16 \mu\text{m}$, are strongly associated with both accretion and ejection processes in YSOs (J. Muzerolle et al. 1998; A. Caratti o Garatti et al. 2016; R. Fedriani et al. 2018). Recently, S. Federman et al. (2024) have shown extended $\text{Br}\alpha$ knots directly associated with outflows from multiple YSOs using JWST-NIRSpec integral field unit observations.

Individual outflow knots are identified by eye as extended features that stand out among the local noise in the continuum-subtracted images, estimated by sampling the standard deviation in a square aperture capturing blank sky in the vicinity of each knot candidate. We impose a minimum resolvable size for each knot candidate based on the angular resolution, which is ~ 3 pixels for each image (F212N, F405N, F470N).

The minimum intensity above the local background to constitute a detection across all filters was set at 10σ owing to the high background emission levels throughout the image. The value of σ varies between ~ 0.3 and 0.5 MJy sr^{-1} (see Table 4) depending on the region and filter. Knots that appear to have distinct substructure are split into parts (e.g., A, B, C, etc.), named in descending order of brightness.

Due to the inherently crowded nature of the CMZ star field, knot candidates were thoroughly cross-matched via visual inspection across all continuum filters to confirm that they are authentic line-emitting structures rather than stars. Table 4 presents a list of all identified knots and the coordinate and flux at their peak pixel.

Table 4 also provides a prediction of the driving source for most knots, including its position angle and angular separation with respect to this source. Associations between individual outflow knots and driving sources were made first based on inspection of the continuum-subtracted images to identify linear patterns that would indicate strings of knots emanating from a single source. These individual associations are used to reconstruct the outflow axis for each source. This analysis revealed more YSOs via associations with outflow knots that are not in Table 3 (i.e., they do not possess a reddened IR counterpart or are not in the ALMA Band 6 data); these are presented in Table 5. Knots within the main Sgr C cloud that

Table 3
Cores from X. Lu et al. (2020) with a Matching NIR Source

ALMA ID	M_{mm} (M_{\odot})	R.A. (J2000)	Decl. (J2000)	$\Delta\theta$ (arcsec)	m_{F480M}	m_{F360M}	m_{F162M}	$m_{\text{F162M}} - m_{\text{F480M}}$
sgrc263	3.44	17:44:42.684	-29:27:35.21	0.007	18.098 ± 0.010	18.421 ± 0.008	22.172 ± 0.014	4.074
sgrc132	1.53	17:44:41.797	-29:28:02.18	0.025	19.081 ± 0.017	>4.119
sgrc12	3.63	17:44:40.274	-29:28:17.28	0.032	17.781 ± 0.008	18.113 ± 0.005	22.272 ± 0.015	4.491
sgrc72 [†]	1.33	17:44:43.584	-29:28:12.18	0.036	16.768 ± 0.004	>6.432
sgrc245	2.47	17:44:40.852	-29:27:44.32	0.038	17.890 ± 0.009	18.606 ± 0.009	23.127 ± 0.020	5.237
sgrc177	13.59	17:44:42.074	-29:27:56.37	0.040	18.495 ± 0.011	18.772 ± 0.008	22.549 ± 0.015	4.054
sgrc261	7.57	17:44:42.678	-29:27:36.86	0.041	16.673 ± 0.004	17.139 ± 0.004	21.127 ± 0.007	4.454
sgrc81 [†]	0.69	17:44:40.304	-29:28:11.23	0.042	15.721 ± 0.009	>7.479
sgrc265	9.38	17:44:43.525	-29:27:32.58	0.044	17.570 ± 0.007	>5.630
sgrc201	0.41	17:44:42.084	-29:27:54.55	0.054	18.259 ± 0.009	18.565 ± 0.007	22.619 ± 0.017	4.360
sgrc259 [†]	1.06	17:44:41.927	-29:27:37.77	0.056	15.829 ± 0.003	>7.371
sgrc41 [†]	2.15	17:44:40.137	-29:28:15.00	0.062	10.876 ± 0.001	13.531 ± 0.001	21.861 ± 0.012	10.985
sgrc9	0.90	17:44:40.667	-29:28:19.13	0.072	20.562 ± 0.068	20.616 ± 0.035	...	>2.638
sgrc264	5.25	17:44:43.498	-29:27:33.11	0.074	17.204 ± 0.005	>5.996
sgrc14	7.34	17:44:40.438	-29:28:17.28	0.081	17.224 ± 0.005	17.461 ± 0.004	20.482 ± 0.004	3.258
sgrc175	1.26	17:44:41.354	-29:27:56.61	0.084	16.770 ± 0.004	18.169 ± 0.005	22.346 ± 0.015	5.576
sgrc217	0.98	17:44:42.327	-29:27:53.23	0.084	17.337 ± 0.006	...	21.720 ± 0.008	4.383
sgrc48 [†]	1.09	17:44:40.537	-29:28:14.63	0.088	12.289 ± 0.001	>10.911
sgrc115	57.71	17:44:41.707	-29:28:03.42	0.089	18.578 ± 0.012	>4.622
sgrc205	11.91	17:44:42.184	-29:27:54.26	0.091	19.117 ± 0.019	19.213 ± 0.010	23.206 ± 0.024	4.089
sgrc238	0.90	17:44:42.541	-29:27:49.13	0.099	20.153 ± 0.041	...	24.844 ± 0.076	4.691
sgrc10	0.54	17:44:40.733	-29:28:18.95	0.099	18.730 ± 0.014	19.576 ± 0.015	23.921 ± 0.045	5.191
sgrc196	22.57	17:44:42.152	-29:27:54.68	0.100	19.150 ± 0.020	19.706 ± 0.017	23.386 ± 0.028	4.236

Note. ALMA ID refers to the ID assigned in X. Lu et al. (2020). The sources marked with daggers are those with a F162M – F480M color index that deviates from the mean by more than 2σ . M_{mm} represents the estimated core mass from X. Lu et al. (2020). Coordinates represent the position of the F480M source. $\Delta\theta$ is the angular separation between the ALMA peak and the F480M source. The magnitudes of sources that are undetected in a given filter are indicated by ellipses. Lower limits on color were calculated using the completeness limit for the F162M catalog: $m_{\text{F162M}} = 23.2$.

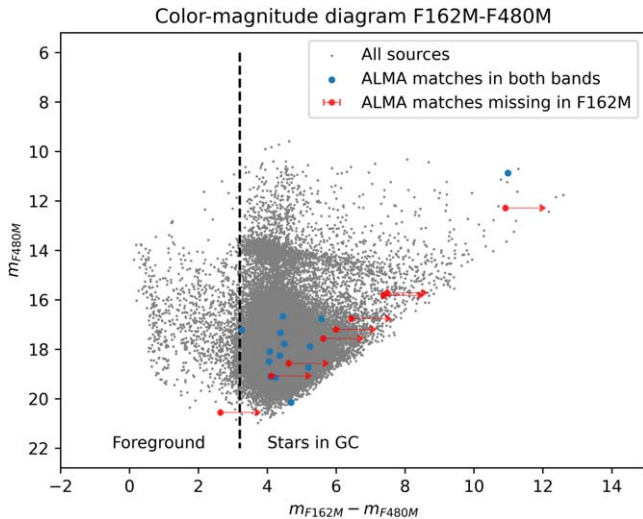


Figure 4. Color–magnitude diagram showing the F162M – F480M color index vs. F480M magnitude. Gray circles represent the sources in the F480M catalog that have a F162M match. Blue circles represent the subset of these that match an ALMA peak. The red circles with arrows represent the F480M sources that have an ALMA match but are undetected in F162M. Their F162M magnitude has been replaced with the completeness limit $m = 23.2$ to obtain a lower limit on the color index. The dashed line at $m_{\text{F162M}} - m_{\text{F480M}} = 3.2$ represents the color cut separating foreground stars from CMZ stars (F. Noguera-Lara 2024).

cannot be assigned a driving source based on linear associations with other knots are simply assigned the closest source from Table 3 that satisfies the reddening requirements described in Section 3.3. These are marked with an asterisk in

Table 4. Knots outside the main Sgr C cloud that still appear to be associated with protostars within the cloud are designated “Sgr C” as their driving source. A similar approach is taken for outflow knots in the star-forming region G359.42–0.104 (see Section 3.5) that cannot be traced back to either of the two identified protostars in that region, G359.42a and G359.42b; these are designated “G359.42–0.104” as their driving source.

Three sources presented in Table 5, G359.44a, G359.44b, and G359.42a, are also characterized in 3 mm Band 3 ALMA continuum data (Section 2.3), and the source coordinates, fluxes, and areas are derived via 2D Gaussian fitting. The fluxes are derived by integrating within $1.5 \times \text{FWHM}$ of the fitted Gaussian ellipse. We also estimate masses for each source using standard assumptions of optically thin thermal emission from dust, i.e.,

$$M_{\text{mm}} = \frac{R_{g/d} S_{\nu} d^2}{\kappa_{\nu} B_{\nu}(T_{\text{dust}})}, \quad (1)$$

where S_{ν} is the dust continuum flux at the frequency ν (100 GHz for Band 3); d is the distance to Sgr C, which we take to be 8.15 kpc (M. J. Reid et al. 2019); κ_{ν} is the dust opacity per unit mass, which we take to be $0.18 \text{ cm}^2 \text{ g}^{-1}$ for Band 3 based on the “OH5” model (V. Ossenkopf & T. Henning 1994) that has been extended to longer wavelengths in C. H. Young & N. J. Evans (2005); and B_{ν} is the spectral radiance (Planck function) at the frequency ν and dust temperature T_{dust} , which is taken to be 20 K, similar to other studies of cores in Sgr C (X. Lu et al. 2020; A. V. I. Kinman et al. 2024). A caveat to note is that the mass estimate is relatively sensitive to the value of temperature, which is uncertain at these small scales (see

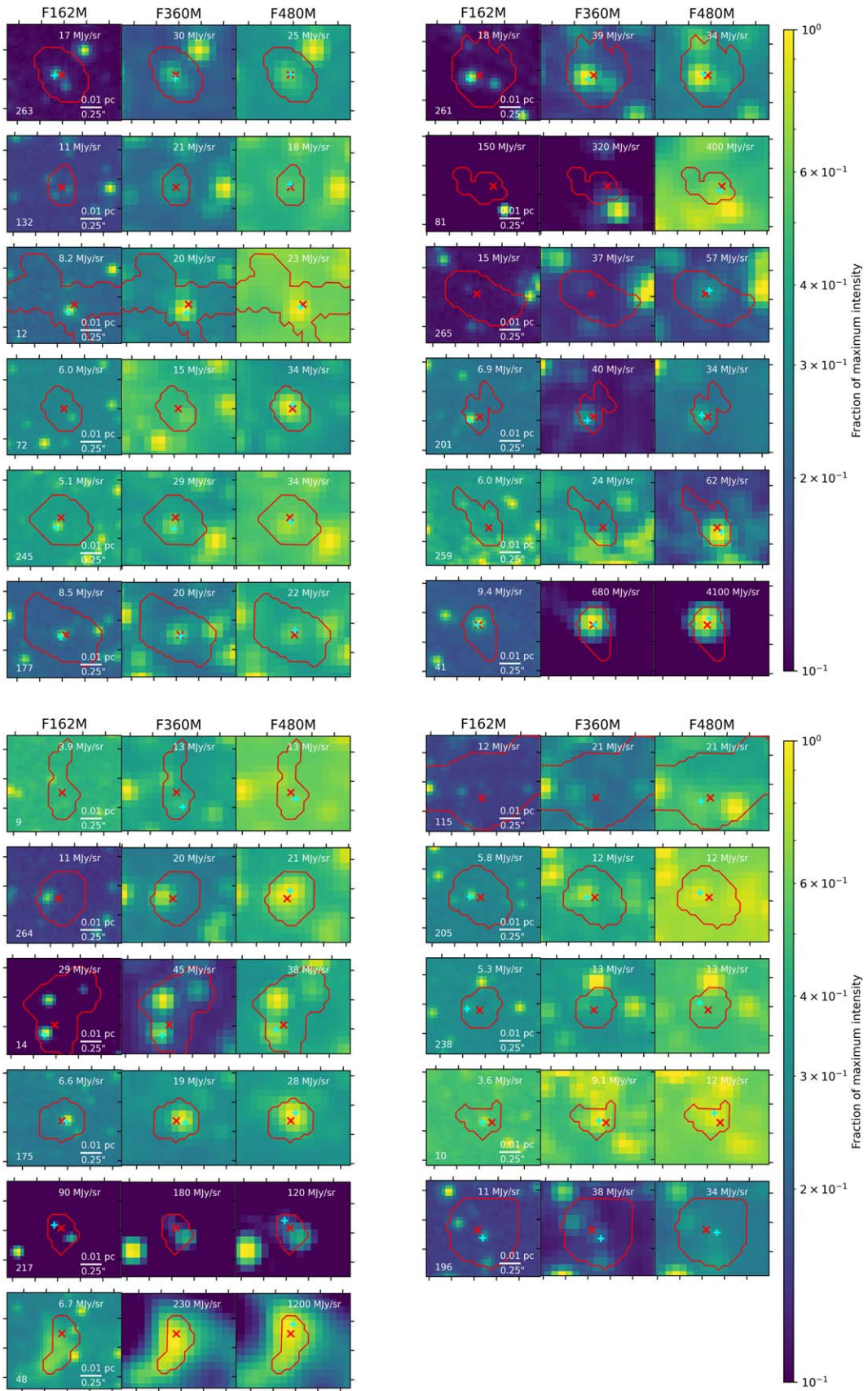


Figure 5. All ALMA cores with matching NIR sources. The background images are NIRCam images in the F162M, F360M, and F480M bands. Red contours and crosses represent the dendrogram contours and 1.3 mm peaks, respectively. The cyan plus signs mark matching NIR sources in the respective images. The indices in the lower left corners are the core IDs listed in Table 3. The color scale has been normalized to the maximum intensity in each image, which is shown in the upper right corner of each panel.

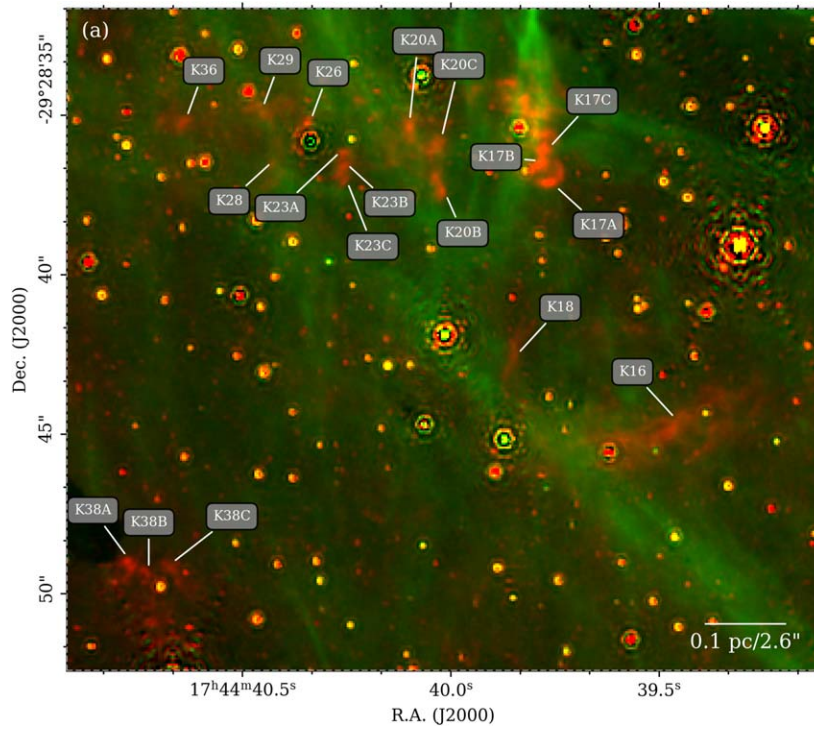
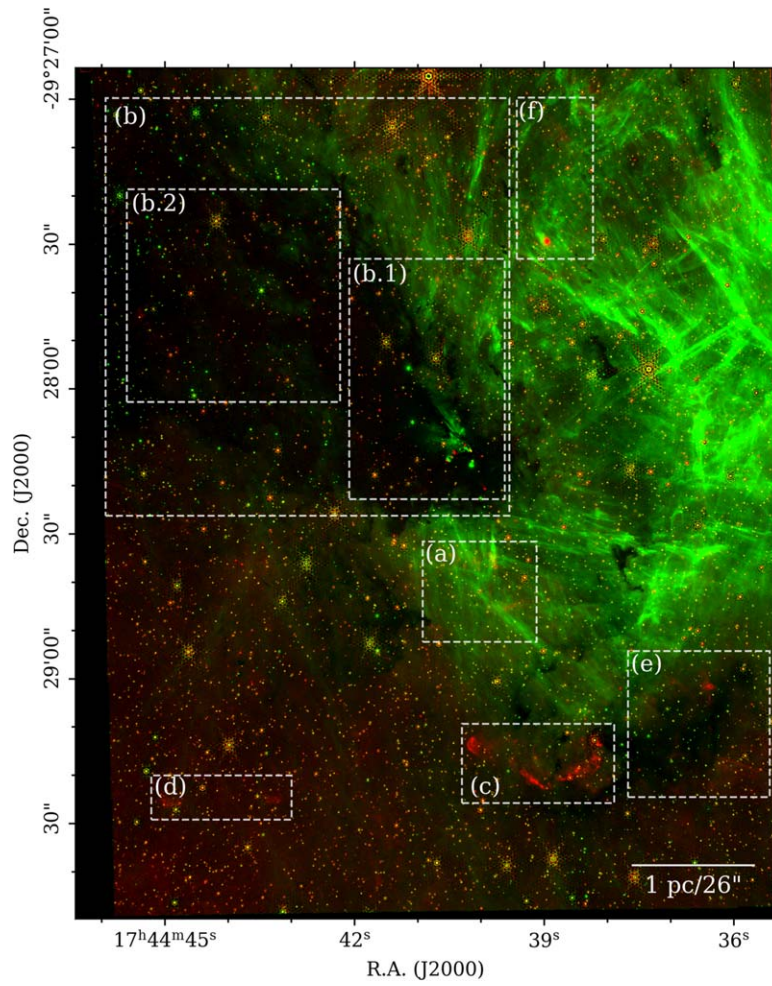


Figure 6. Diagram of the NIRCcam data showing the Sgr C cloud and its surroundings. Red represents F470N and green F405N, both continuum subtracted. The boxes with letters represent cutaways presented in the following figures. North is up and east is to the left in all panels. (a) Magnification of the region to the south of the main protocluster.

Table 4
Knot Features

Feature	R.A. (J2000)	Decl. (J2000)	F_{470} (MJy sr ⁻¹)	F_{212} (MJy sr ⁻¹)	F_{405} (MJy sr ⁻¹)	Source	P.A. (deg)	$\Delta\theta$ (arcsec)	σ_{470} (MJy sr ⁻¹)	σ_{212} (MJy sr ⁻¹)	σ_{405} (MJy sr ⁻¹)	Box
K19A	17:44:39.93	-29:28:20.75	49.56	G359.44a	201	8.32	0.32	(b.1.1)
K19B	17:44:39.99	-29:28:19.83	7.53	"	198	7.19	0.32	(b.1.1)
K19C	17:44:40.02	-29:28:19.08	6.68	"	196	6.36	0.32	(b.1.1)
K22	17:44:40.25	-29:28:12.18	...	13.19	155.89	"	58	1.46	...	0.37	0.41	(b.1.3)
K24	17:44:40.25	-29:28:11.54	27.09	"	41	1.90	0.32	(b.1.3)
K31	17:44:40.45	-29:28:01.91	10.99	"	19	11.68	0.32	(b.1.3)
K33A	17:44:40.50	-29:27:58.78	13.89	"	17	14.86	0.32	(b.1)
K33B	17:44:40.49	-29:27:59.15	11.28	"	17	14.48	0.32	(b.1)
K35	17:44:40.58	-29:27:49.80	18.65	"	13	23.81	0.32	(b.1)
K37	17:44:40.68	-29:27:37.12	28.59	"	11	36.49	0.32	(b.1)
K27A	17:44:40.41	-29:28:13.17	88.43	G359.44b	321	3.56	0.32	(b.1.3)
K27B	17:44:40.42	-29:28:12.92	81.49	"	326	3.65	0.32	(b.1.3)
K27C	17:44:40.37	-29:28:13.34	27.63	"	313	3.82	0.32	(b.1.3)
K27D	17:44:40.47	-29:28:13.75	23.24	"	326	2.65	0.32	(b.1.3)
K30	17:44:40.45	-29:28:13.29	...	15.17	44.88	"	327	3.17	...	0.37	0.41	(b.1.3)
K32	17:44:40.48	-29:28:14.07	...	40.01	67.29	"	325	2.29	...	0.37	0.41	(b.1.3)
K34A	17:44:40.54	-29:28:14.91	76.79	61.68	210.23	"	334	1.16	0.32	0.37	0.41	(b.1.3)
K34B	17:44:40.56	-29:28:15.42	20.95	"	334	0.60	0.32	(b.1.3)
K39	17:44:40.82	-29:28:19.09	5.83	"	135	4.42	0.27	(b.1)
K40	17:44:40.90	-29:28:21.01	5.72	"	141	6.53	0.27	(b.1)
K25	17:44:40.32	-29:28:02.56	5.32	sgrc81*	2	8.69	0.32	(b.1.3)
K41A	17:44:41.04	-29:27:56.95	6.81	"	34	17.28	0.32	(b.1.2)
K41B	17:44:40.99	-29:27:56.74	6.46	"	32	17.04	0.32	(b.1.2)
K41C	17:44:40.92	-29:27:55.96	5.24	"	28	17.29	0.32	(b.1.2)
K42	17:44:41.34	-29:28:01.32	7.36	"	54	16.79	0.27	(b.1)
K43A	17:44:41.52	-29:28:13.22	6.88	sgrc48*	84	12.99	0.27	(b.1)
K43B	17:44:41.54	-29:28:14.17	5.92	"	88	13.14	0.27	(b.1)
K44	17:44:41.69	-29:28:02.38	5.11	"	51	19.48	0.27	(b.1)
K46	17:44:41.95	-29:28:10.40	5.15	"	77	19.00	0.27	(b.1)
K45	17:44:41.94	-29:27:56.11	7.29	sgrc259*	179	18.32	0.27	(b.1)
K47	17:44:42.64	-29:27:39.15	5.06	"	98	9.50	0.25	(b.2)
K48	17:44:43.44	-29:27:26.13	6.98	"	59	22.92	0.25	(b.2)
K49	17:44:43.52	-29:27:30.50	4.50	"	71	22.06	0.25	(b.2)
K50	17:44:43.69	-29:27:34.65	9.04	"	82	23.26	0.25	(b.2)
K51	17:44:43.75	-29:27:34.60	8.40	"	82	24.01	0.25	(b.2)
K52	17:44:43.79	-29:27:20.96	6.31	"	55	29.59	0.25	(b.2)
K54	17:44:44.03	-29:27:31.86	10.20	"	78	28.15	0.25	(b.2)
K53	17:44:43.93	-29:27:58.33	4.45	sgrc72*	18	14.60	0.25	(b.2)
K55A	17:44:44.81	-29:27:51.45	19.19	"	38	26.26	0.24	(b.2)
K55B	17:44:44.79	-29:27:51.94	12.07	"	38	25.71	0.24	(b.2)
K56	17:44:45.28	-29:27:42.72	7.96	"	37	36.92	0.24	(b.2)
K57	17:44:45.37	-29:27:45.02	14.56	"	41	35.80	0.24	(b.2)
K16	17:44:39.47	-29:28:44.84	15.36	Sgr C	?	?	0.49	(a)
K17A	17:44:39.77	-29:28:37.13	29.71	"	?	?	0.49	(a)
K17B	17:44:39.79	-29:28:36.57	26.40	"	?	?	0.49	(a)
K17C	17:44:39.78	-29:28:36.13	23.36	"	?	?	0.49	(a)
K18	17:44:39.85	-29:28:42.25	11.08	"	?	?	0.49	(a)

Table 4
(Continued)

Feature	R.A. (J2000)	Decl. (J2000)	F_{470} (MJy sr ⁻¹)	F_{212} (MJy sr ⁻¹)	F_{405} (MJy sr ⁻¹)	Source	P.A. (deg)	$\Delta\theta$ (arcsec)	σ_{470} (MJy sr ⁻¹)	σ_{212} (MJy sr ⁻¹)	σ_{405} (MJy sr ⁻¹)	Box
K20A	17:44:40.10	-29:28:35.41	18.85	"	?	?	0.49	(a)
K20B	17:44:40.02	-29:28:37.40	17.77	"	?	?	0.49	(a)
K20C	17:44:40.03	-29:28:35.96	15.19	"	?	?	0.49	(a)
K23A	17:44:40.25	-29:28:36.16	15.91	"	?	?	0.49	(a)
K23B	17:44:40.25	-29:28:36.60	15.31	"	?	?	0.49	(a)
K23C	17:44:40.26	-29:28:37.10	13.04	"	?	?	0.49	(a)
K26	17:44:40.34	-29:28:35.24	20.10	"	?	?	0.49	(a)
K28	17:44:40.43	-29:28:36.53	11.02	"	?	?	0.49	(a)
K29	17:44:40.45	-29:28:34.96	13.68	"	?	?	0.49	(a)
K36	17:44:40.65	-29:28:35.34	13.55	"	?	?	0.49	(a)
K38A	17:44:40.77	-29:28:48.98	17.14	"	?	?	0.49	(a)
K38B	17:44:40.74	-29:28:49.28	13.21	"	?	?	0.49	(a)
K38C	17:44:40.67	-29:28:49.20	12.21	"	?	?	0.49	(a)
K2	17:44:38.13	-29:29:13.67	54.38	17.00	...	G359.42a	208	1.01	0.43	0.28	...	(c)
K15	17:44:39.46	-29:29:13.04	23.21	10.25	...	"	91	16.87	0.43	0.28	...	(c)
K21A	17:44:40.13	-29:29:12.50	33.76	11.91	...	"	89	25.64	0.43	0.28	...	(c.3)
K21B	17:44:40.18	-29:29:14.59	31.96	15.80	...	"	94	26.28	0.43	0.28	...	(c.3)
K9	17:44:38.91	-29:29:19.84	11.14	G359.42b	290	3.56	0.43	(c)
K10A	17:44:39.04	-29:29:18.88	10.32	"	322	2.76	0.43	(c.2)
K10B	17:44:39.14	-29:29:18.97	9.56	"	349	2.13	0.43	(c.2)
K11	17:44:39.04	-29:29:22.15	33.03	5.72	...	"	236	1.97	...	0.28	...	(c.2)
K12A	17:44:39.12	-29:29:21.48	52.94	20.39	...	"	238	0.80	0.43	0.28	...	(c.2)
K12B	17:44:39.11	-29:29:21.66	...	19.41	...	"	233	0.98	...	0.28	...	(c.2)
K12C	17:44:39.14	-29:29:21.20	...	12.80	...	"	249	0.39	...	0.28	...	(c.2)
K13	17:44:39.17	-29:29:21.06	168.48	144.64	...	"	102	0.09	0.43	0.28	...	(c.2)
K14	17:44:39.32	-29:29:19.92	22.57	5.58	...	"	60	2.31	0.43	0.28	...	(c.2)
K1	17:44:37.99	-29:29:20.92	12.76	G359.42-0.104	?	?	0.43	(c.1)
K3A	17:44:38.14	-29:29:18.20	24.65	7.14	...	"	?	?	0.43	0.28	...	(c.1)
K3B	17:44:38.14	-29:29:18.14	...	6.17	...	"	?	?	...	0.28	...	(c.1)
K4	17:44:38.19	-29:29:23.32	11.10	"	?	?	0.43	(c.1)
K5A	17:44:38.20	-29:29:16.27	28.81	15.60	...	"	?	?	0.43	0.28	...	(c.1)
K5B	17:44:38.22	-29:29:16.59	24.02	5.84	...	"	?	?	0.43	0.28	...	(c.1)
K5C	17:44:38.15	-29:29:16.32	19.11	"	?	?	0.43	(c.1)
K5D	17:44:38.19	-29:29:16.74	...	6.30	...	"	?	?	...	0.28	...	(c.1)
K5E	17:44:38.19	-29:29:17.06	...	6.54	...	"	?	?	...	0.28	...	(c.1)
K6A	17:44:38.30	-29:29:18.07	19.68	8.57	...	"	?	?	0.43	0.28	...	(c.1)
K6B	17:44:38.36	-29:29:18.91	18.97	"	?	?	0.43	(c.1)
K6C	17:44:38.31	-29:29:19.20	14.14	"	?	?	0.43	(c.1)
K7A	17:44:38.49	-29:29:19.20	26.99	7.47	...	"	?	?	0.43	0.28	...	(c.1)
K7B	17:44:38.57	-29:29:18.53	14.71	"	?	?	0.43	(c.1)
K8	17:44:38.70	-29:29:20.84	25.08	"	?	?	0.43	(c.1)

Note. Coordinates and peak fluxes are given from the highest value pixel of the knot. Candidate driving sources are given in Tables 3 and 5. Knots that are not at a high enough σ peak above their local background (see Section 3.4) to constitute a detection (or are unresolvable at a given wavelength) are indicated by ellipses. Sources are grouped by driving source and are ordered in ascending order of R.A. for each source. The name of the box showing each knot in Figures 6–8 is given.

Table 5

Outflow Sources That Were Not Identified in the JWST + ALMA Source Cross-matching (Section 3.3), but Rather by Association to Nearby Outflow Knots in Atomic/Molecular Hydrogen Emission (See Table 4)

Source Name	R.A. (J2000)	Decl. (J2000)	S_3 (mJy)	S_6 (mJy)	M_{mm} (M_{\odot})	Area (arcsec ²)
G359.44a ^a	17:44:40.11	−29:28:13.05	19.4	102.7	629.7/154.8	9.8
G359.44b ^b	17:44:40.55	−29:28:16.08	40.8	201.53	1321.4/303.7	17.7
G359.42a	17:44:38.17	−29:29:12.75	2.8	...	89.7	6.6
G359.42b	17:44:39.15	−29:29:21.14

Notes. Coordinates for G359.44a, G359.44b, and G359.42a are given from 2D Gaussian fitting in the Band 3 continuum image; coordinates for G359.42b, which is not visible in the Band 3 image, are given from the estimated geometric center of its outflow cone visible in the NIRCcam image. The associated coordinates, flux, and mass of G359.44a and G359.44b from 1.3 mm Band 6 data analyzed by X. Lu et al. (2020) are also given; the masses are given first from Band 3 and second from Band 6 and are separated by a slash.

^a R.A. and decl. from Band 6 data: 17:44:40.16–29:28:12.95.

^b R.A. and decl. from Band 6 data: 17:44:40.60–29:28:15.91.

X. Lu et al. 2020, for further discussion); if a value of 50 K is used, the mass estimates would decrease by a factor of ~ 3 . A gas-to-dust ratio of 100 was adopted following V. Ossenkopf & T. Henning (1994), i.e., a value of $R_{g/d} = 101$ (to account for the additional 1 part in 100 of dust). It is important to note that these values represent primarily the masses of the envelopes of the protostar candidates, rather than the masses of the protostars themselves. Additionally, the mass estimates for Band 3 are likely overestimated owing to the strong presence of free–free emission at 3 mm, which we have ignored by assuming that all emission around the protostars is thermal emission from dust. Therefore, the Band 3 mass estimates presented in Table 5 should be interpreted as upper limits.

Figures 6–8 show diagrams of the locations of each identified knot. Appendix B presents a highly magnified “significance map” of each knot, where contours are shown representing increments of the standard deviation of the local background, indicating the statistical significance of each knot. There are also a number of line-emitting objects that appear unrelated to star formation activity. Appendix C presents a compilation of such miscellaneous molecular hydrogen objects (MHOs) that are not spatially coincident with any star-forming regions.

3.5. A Newly Discovered Star-forming Region: G359.42–0.104

The JWST data reveal H_2 line emission features indicating star formation activity $\sim 1'$ to the south of the main Sgr C protocluster (see Figure 1 and region (c) in Figure 6). We name this star-forming region G359.42–0.104. Figure 8 shows a magnification of this region, revealing several bright H_2 features, including a large bow shock, knot 21, to the east. In general, these shocks tend to “curve back” in the direction of their driving source; in this case, knot 21B (shown magnified in box (c.3) of Figure 8) points directly back (along the same line as knot 15) to a driving source, which we name G359.42–0.104-a (hereafter G359.42a).

G359.42a is the site of a bright ALMA Band 3 continuum peak ($M_{\text{mm}} \simeq 90M_{\odot}$; Table 5), as well as a water maser emission detected in X. Lu et al. (2019b), labeled by those authors as W16. This water maser has a peak velocity close to 0 km s^{-1} , which contrasts with the velocity of the masers in the Sgr C cloud at approximately -60 km s^{-1} . This difference may

indicate that this source is not part of the Sgr C cloud, although the velocity is still consistent with being within the CMZ.

Knot 21A may be an overdensity in flux in the main bow shock, knot 21B, or it may represent another bow shock entirely that points toward the bright emission in the south, magnified in panel (c.2) of Figure 8. We speculate that a driving source, G359.42–0.104-b (hereafter G359.42b), is located in this complex, although it is not associated with an ALMA Band 3 dust continuum peak. Given that the mass limit of the ACES observations is $\sim 10 M_{\odot}$ (S. Longmore 2024, private communication), it is altogether possible that the millimeter counterpart is simply too low in mass to be detected in the Band 3 data. The coordinates of G359.42b given in Table 5 and indicated in Figure 8 are taken from the estimated geometric center of the nebulosity/outflow cone in the F212N image.

Additionally, many outflow knots are seen in both F470N and F212N to the southeast of G359.42a (see Figure 8(c.1)). These features likely represent shocked outflow knots from further unresolved YSOs in the region, as they do not appear to lie along the outflow axis of either G359.42a or G359.42b. Inspection of the rest of the short-wavelength filters (i.e., F182M, F162M, and F115W; see Figure 9) reveals a morphology reminiscent of a young, nebulous protocluster, i.e., bright extended emission enshrouding a cluster of (proto) stars, with what may be a cloud to the northwest that is being internally illuminated by the cluster members. Therefore, due to the clustering of line-emitting features in this region, as well as its morphology across the short-wavelength filters, we predict that this is the most likely location of additional YSOs in G359.42–0.104, although it is difficult to predict their exact positions.

It is uncertain whether this region is at the galactocentric distance or is foreground. Although there are several stars with distance estimates from Gaia (Gaia Collaboration et al. 2023) in the vicinity of the cluster shown in Figure 9, it is impossible to disentangle foreground stars from authentic cluster members, especially since there is no noticeable enhancement of Gaia stars in the cluster region. Reddening/extinction measurements are similarly uncertain owing to an inability to reliably differentiate cluster members in the crowded field. Proper motions, which will be available in the coming months from the GALACTICNUCLEUS survey (F. Nogueras-Lara et al. 2018), will be useful in discerning the movement of the cluster members to compare with typical CMZ kinematics.

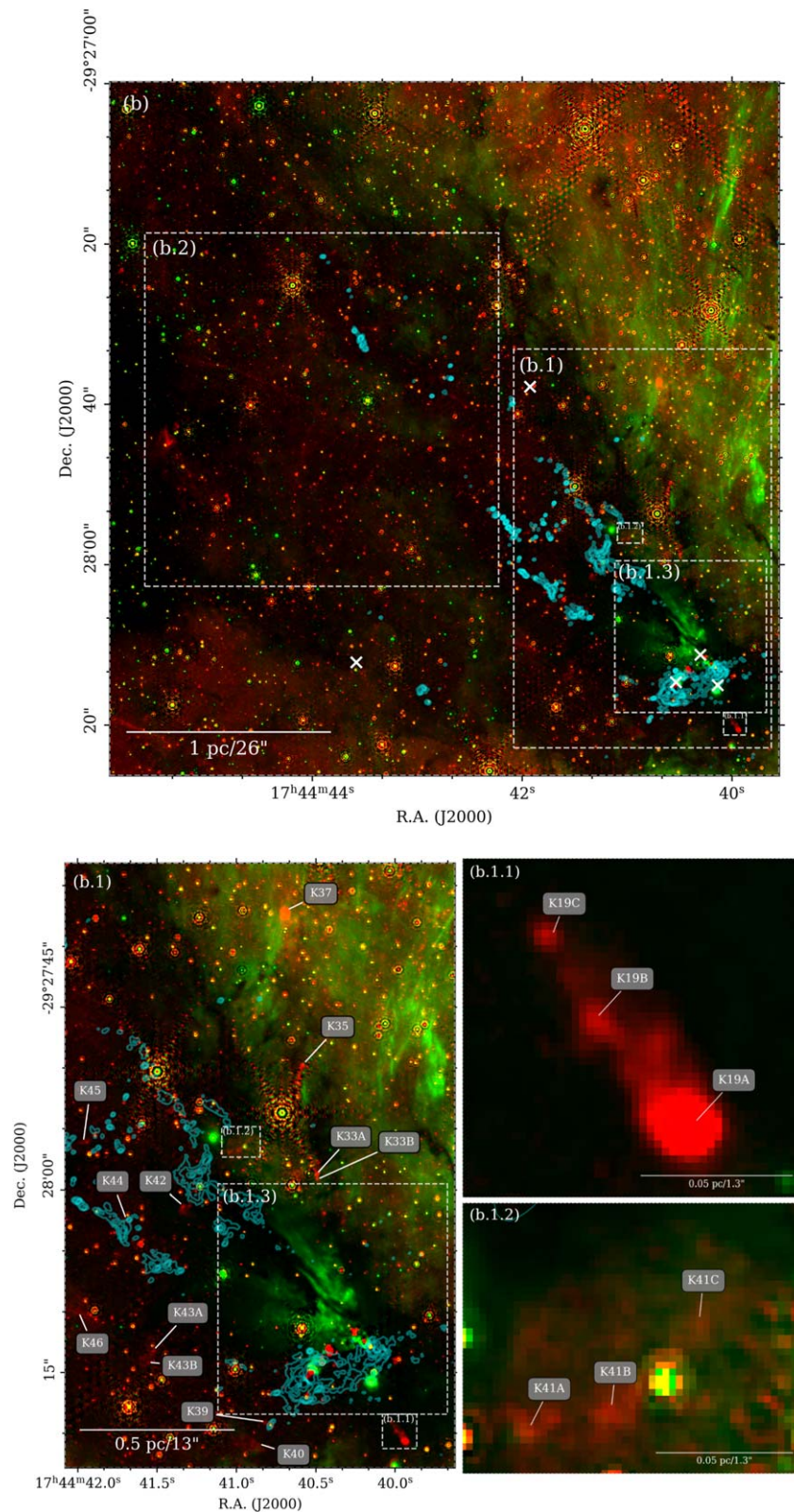


Figure 7. Diagram of the Sgr C molecular cloud. (b) Magnification of the entire cloud, with ALMA Band 6 continuum (X. Lu et al. 2020) contours (masked for primary beam response < 0.4) with 10, 20, 30, 50, 100, 200 \times rms noise of the image. White crosses mark the positions of the five YSO candidates identified in Section 3.3. (b.1) Magnification of the Sgr C protocluster, with outflow knots labeled. The cyan contours are the same as in the previous panels. (b.1.1) Magnification of the knot 19 complex. (b.1.2) Magnification of the knot 41 complex. (b.1.3) Magnification of the inner part of the Sgr C protocluster, with knots and sources labeled. The FOV is the same as Figure 2. Note the “yellow” pixels (e.g., around G359.44a) that are the result of saturation in the F480M image used for subtraction. White stars mark the positions of the massive protostars discussed in the text. White and blue crosses mark the positions of OH masers from W. D. Cotton & F. Yusef-Zadeh (2016) and CH₃OH masers from J. L. Caswell et al. (2010), respectively. Magenta diamonds represent H₂ and Br γ line features observed by S. Kendrew et al. (2013). (b.2) Upper part of the Sgr C dark cloud, with outflow knots and filamentary structures labeled. The contours are the same as in previous panels.

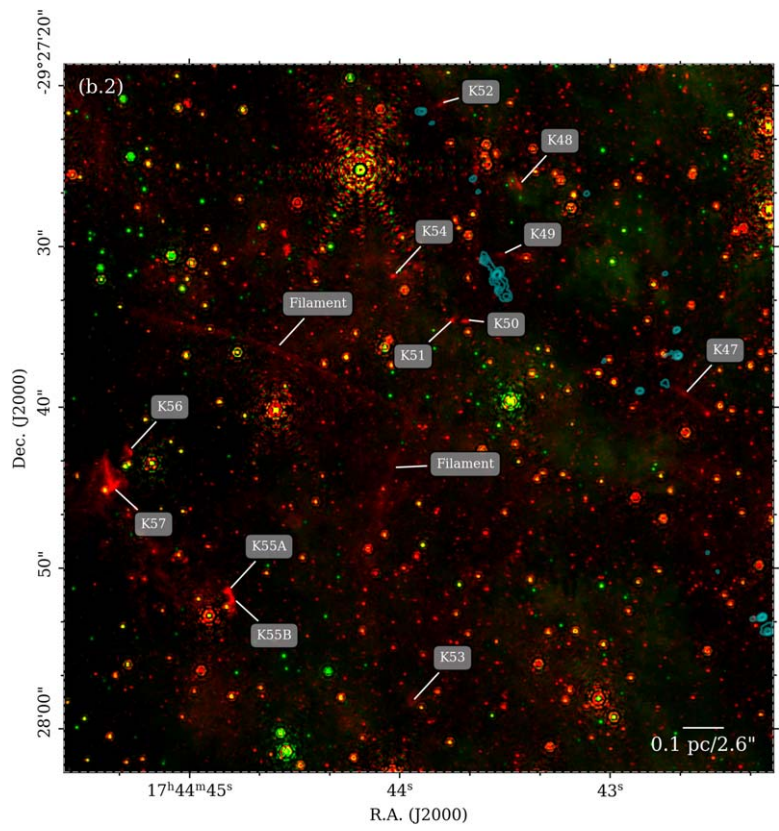
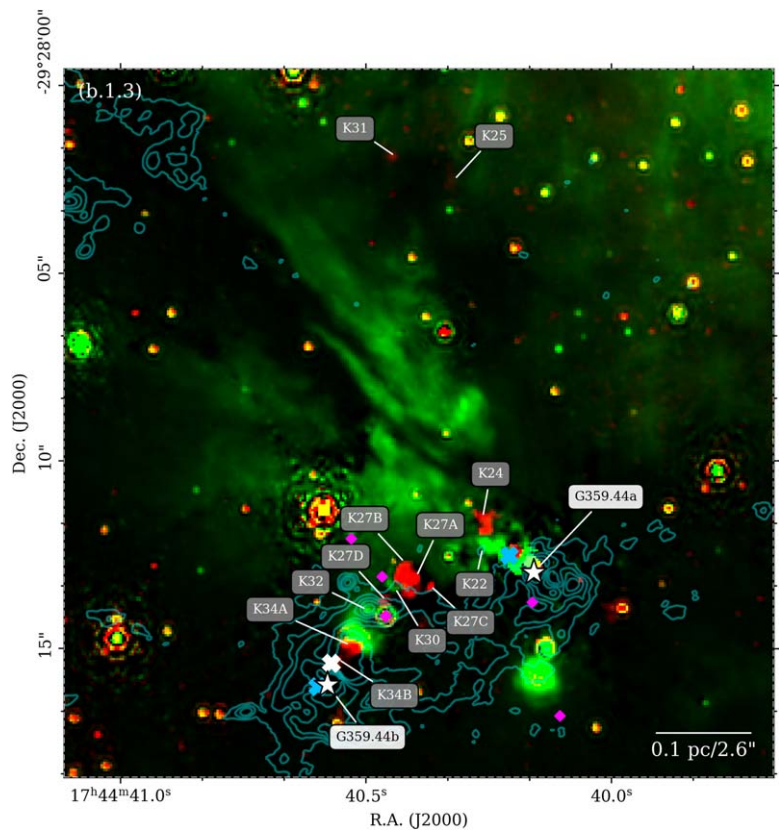


Figure 7. (Continued.)

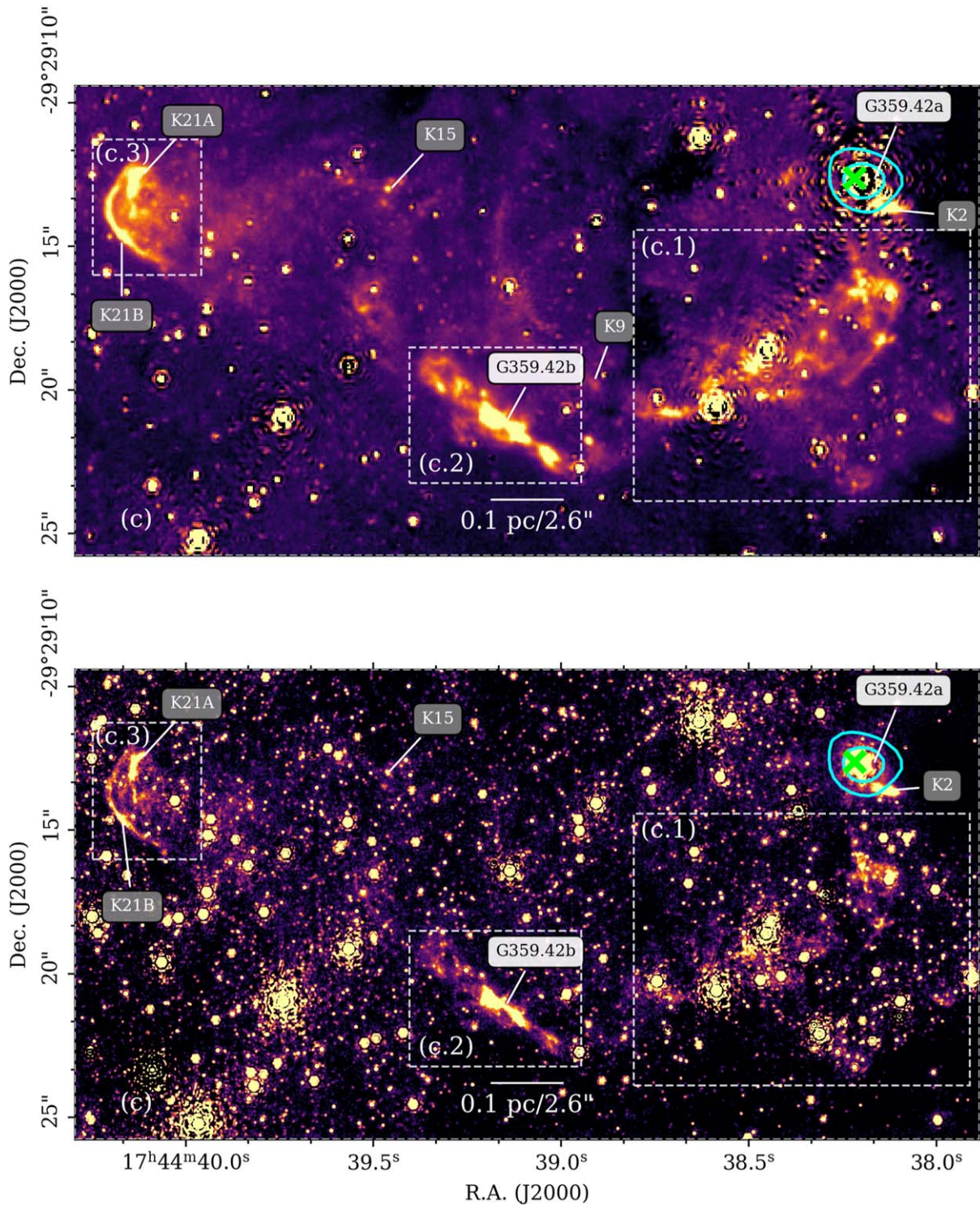


Figure 8. Diagram of the G359.42–0.104 star-forming complex with knots and sources identified and labeled. The FOV is the same as indicated in the first panel of Figure 6. Top: continuum-subtracted F470N data. The cyan contours show 3 mm ALMA continuum data (Section 2.3) and represent $5\times$ and $10\times$ rms noise of the data. The green cross represents the site of a water maser detected in VLA Band C data (X. Lu et al. 2019b). Bottom: F212N continuum-subtracted image. The contours and green cross are the same as in the left panel. Left: magnification of the G359.42b complex as a “significance map” in the style of Appendix B; contours in F470N (top) represent 15σ to 100σ in steps of 5σ above the local background; contours in F212N (bottom) represent 10 to 100σ in steps of 5σ above the local background. Right: magnification of the southwest region of G359.42–0.104, with several bright line-emitting features labeled in both F470N (top) and F212N (bottom). Magnification of the two prominent bow shocks in G359.42–0.104, labeled as 21A and 21B and shown in F470N (left) and F212N (right). The contours in each filter have the same levels as in panel (c.2).

Therefore, we tentatively adopt a distance to this region as the galactocentric distance of 8.15 kpc (M. J. Reid et al. 2019), placing G359.42–0.104 in the CMZ until further evidence is

available. Using this distance, SED fitting was conducted on the protostar G359.42a via similar methods to those described in Section 3.2, but with a single $3/5$ aperture that was

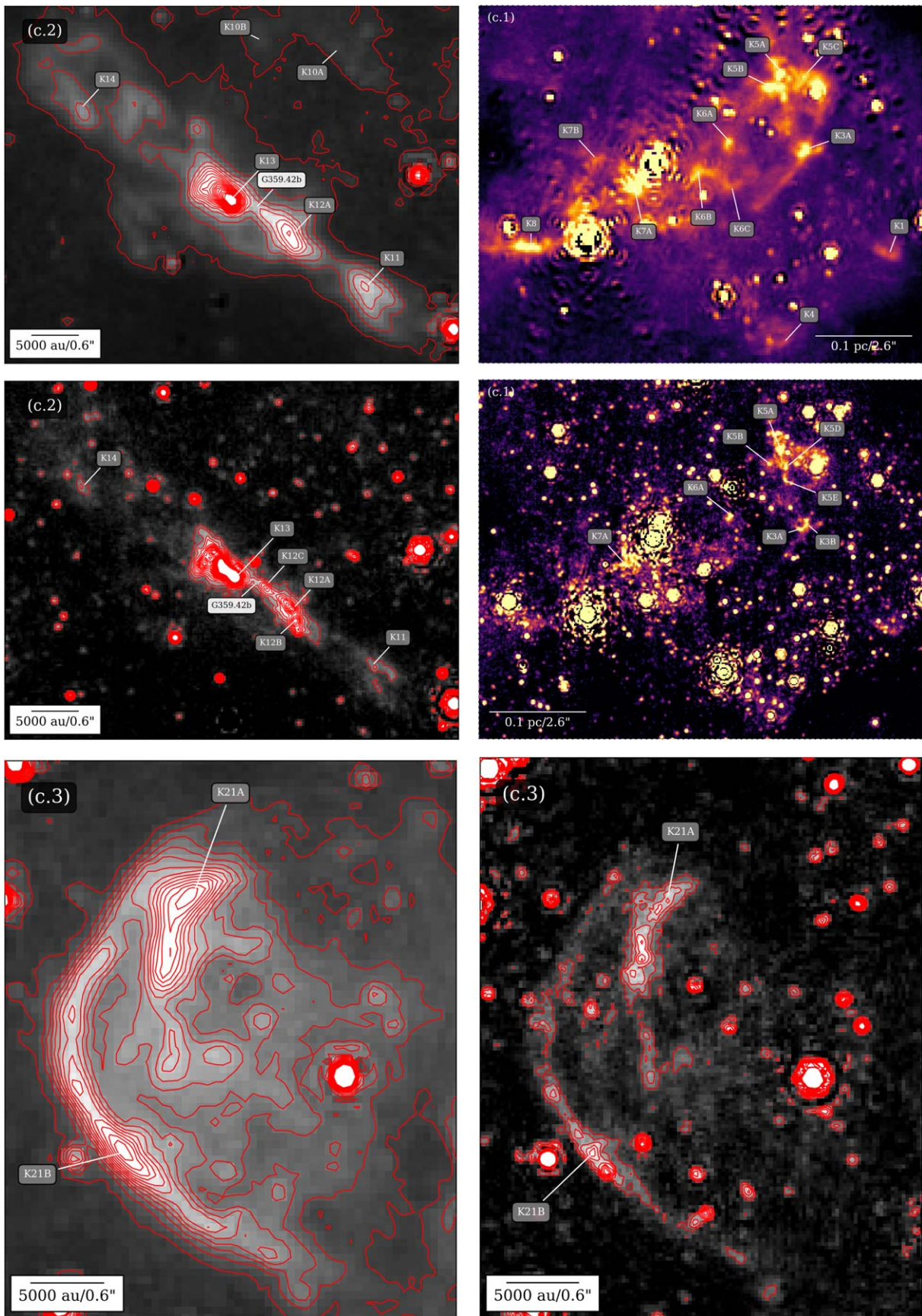


Figure 8. (Continued.)

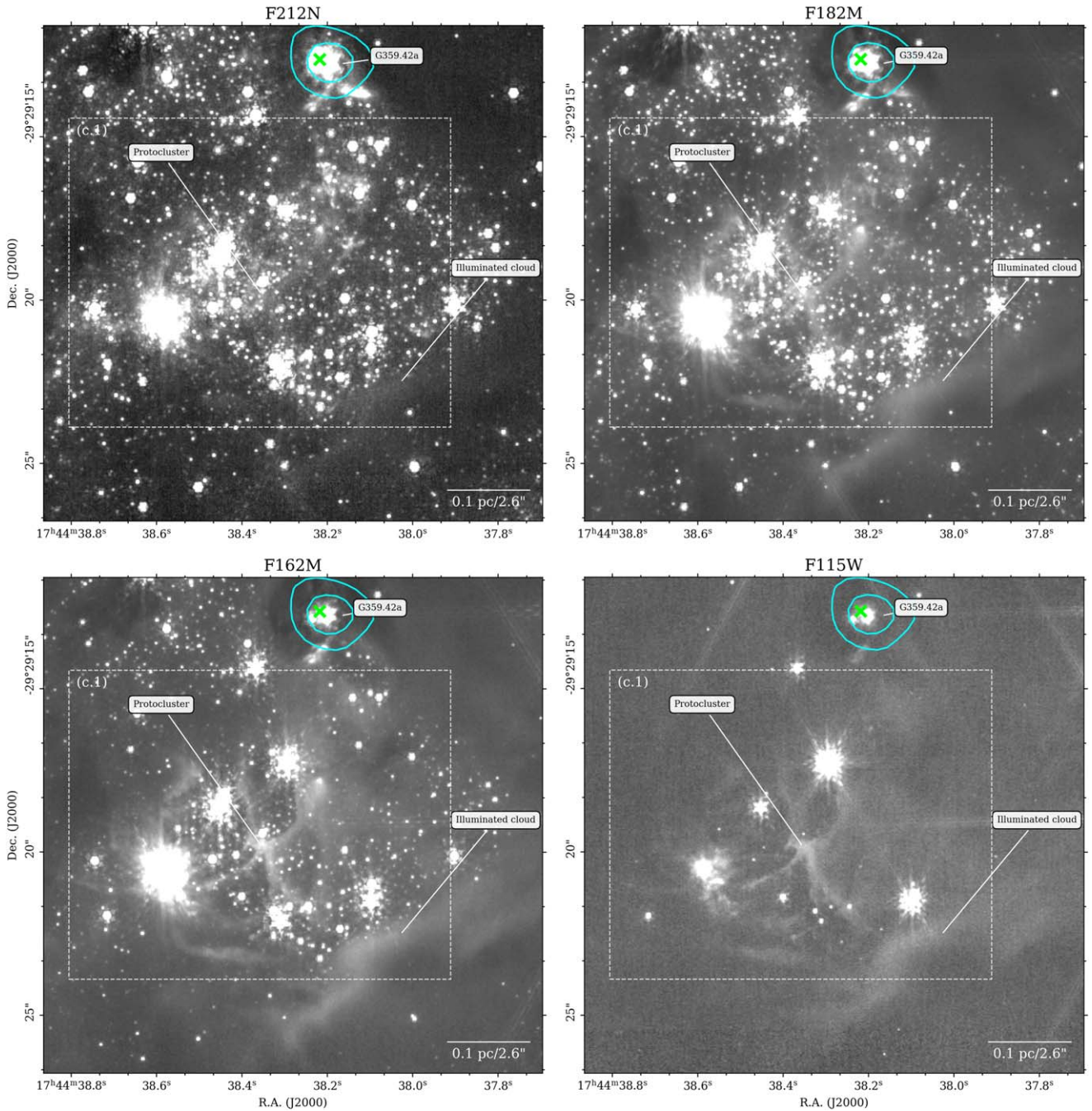


Figure 9. Magnification of the protocluster in G359.42–0.104. The cyan contours show 3 mm ALMA continuum data (Section 2.3) and represent $5\times$ and $10\times$ rms noise of the data. The green cross represents the site of a water maser detected in VLA Band C data (X. Lu et al. 2019b). Box (c.1) from Figure 8 is shown for reference. The protocluster candidate and illuminated cloud discussed in the text are indicated.

algorithmically fit to the source in the SOFIA $37\ \mu\text{m}$ image (see R. Fedriani et al. 2023b, for further details). This aperture was used for photometry across all wavelengths. An eight-panel image showing G359.42a from the NIR to FIR, along with its SED and 2D parameter space plot, is shown in Figure 10.

4. Discussion

4.1. Massive Star Formation in Sgr C

Star formation in the Sgr C cloud is dominated by two massive protostars, G359.44a and G359.44b, separated by $\sim 5''$ (i.e., ~ 0.2 pc). The SED-fitted mass for G359.44a, $20.7^{+14.1}_{-8.4} M_{\odot}$ (see

Section 3.2 and Table 2), is in good agreement, within uncertainties, with the measurement of $m_{*} = 31.7 \pm 4.7 M_{\odot}$ made by X. Lu et al. (2022) based on the dynamical mass inferred by rotation velocities in its protostellar disk. The bolometric luminosity, $L_{\text{bol}} = 9.7^{+15.6}_{-6.0} \times 10^4 L_{\odot}$, and disk mass, $M_{\text{disk}} = 6.9^{+4.7}_{-2.8} M_{\odot}$, for G359.44a predicted by SED fitting are also in good agreement with the measurements made by X. Lu et al. (2022) with ALMA of $L_{\text{bol}} \gtrsim 10^5 L_{\odot}$ and $M_{\text{disk}} = 4.7^{+4.7}_{-2.35} M_{\odot}$, corroborating that G359.44a is indeed a massive protostar and placing independent constraints on its physical parameters.

G359.44b, on the other hand, appears to be a much more deeply embedded, though perhaps eventually more massive,

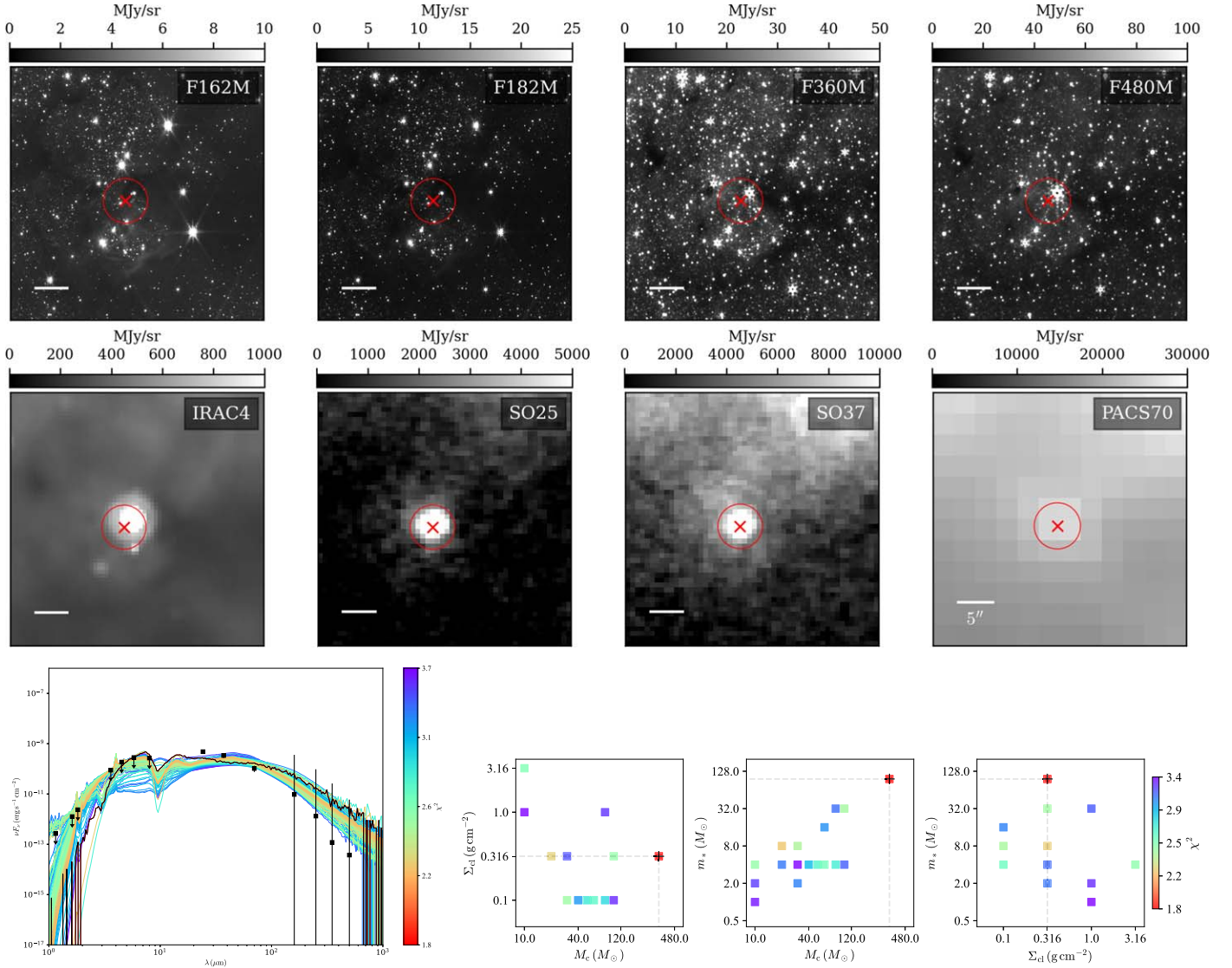


Figure 10. Top: eight-panel image of the protostar G359.42a in NIR and MIR filters. In all panels north is up and east is to the left. Bottom left: protostellar SED for G359.42a, with SED fittings overlaid and color-coded by χ^2 , with the best-fit SED as a black line. Bottom right: 2D parameter space plots for the fitting results on G359.42a. Various parameter pairings are given on the x- and y-axes of each plot, with each pairing of parameter values color-coded by χ^2 . Dashed gray lines indicate the lowest χ^2 (i.e., best-fitting) pair of parameter values.

protostar. Although the NIR to FIR emission in Sgr C is dominated by G359.44a, itself a bright infrared source (see, e.g., Figure 2), G359.44b is much brighter in millimeter wavelengths, being associated with a millimeter core that has almost double the ALMA Band 6 1.3 mm flux (and therefore inferred mass; $M_{\text{mm}} = 303.7 M_{\odot}$) as G359.44a ($M_{\text{mm}} = 154.8 M_{\odot}$). The same trend is seen in ALMA Band 3 (3 mm) data (Table 5). G359.44b is also associated with a methanol maser almost two orders of magnitude brighter than that associated with G359.44a (J. L. Caswell et al. 2010), as well as an OH maser (W. D. Cotton & F. Yusef-Zadeh 2016). SED fitting on both protostars (Section 3.2) indicates that although they have nearly identical masses, G359.44b is more luminous, younger, embedded in a more massive envelope, and surrounded by a denser environment than G359.44a (see Table 2). These differences are within the error bounds on each measurement; however, they are consistent with the other available evidence in indicating that G359.44b either is currently more massive than G359.44a or will be after its formation.

There is also evidence for other, slightly more evolved YSOs in the vicinity of G359.44a and G359.44b. The F405N (Br α) filter shows three bright ultracompact (UC) H II regions in the vicinity of the protostars, each surrounding a point source in the NIRCcam data (see Figure 11). Two of these match with Very Large Array (VLA) Band C (6 cm) UC H II regions in X. Lu et al. (2019a), C102 and C103. The presence of UC H II regions surrounding young, ionizing massive stars in the vicinity of these massive protostars implies that multiple generations of star formation have occurred and are coexisting in Sgr C; this is further corroborated by the extended, mature Sgr C H II region (with an age of ~ 4 Myr; J. P. Simpson 2018) and the detection of $>10^5 M_{\odot}$ of young stars in the Sgr C region by F. Nogueras-Lara (2024), which have an estimated age of ~ 20 Myr.

The stellar density in the region can also be estimated. This has been put forward as a potential metric for assessing the formation conditions of massive protostars, in particular in determining the degree of YSO crowding in the vicinity of these protostars to compare with massive star formation models

(see, e.g., S. Crowe et al. 2024). Within a $9''$ (0.35 pc) radius of G359.44a, the source that appears to be central in the nebosity defining the protocluster region, the surface density of sources identified in F480M that are invisible in F115W (and therefore more likely to be protocluster members owing to the high levels of extinction toward Sgr C) is $\sim 2600 \text{ pc}^{-2}$. The surface density of millimeter dust cores identified by X. Lu et al. (2020), which represent additional YSO candidates not visible in the IR, is $\sim 400 \text{ pc}^{-2}$. Therefore, the total YSO candidate surface density surrounding G359.44a is $\sim 3000 \text{ pc}^{-2}$. However, it must be acknowledged that many of the IR sources identified are likely spurious detections (i.e., foreground/background sources), rather than YSOs associated with the Sgr C protocluster, due to the highly crowded nature of CMZ star fields. Furthermore, the bright and extended nebosity surrounding G359.44a limits the detection of sources in this region to only the brightest objects, further limiting the completeness of the source counts (and meaning that the mass sensitivity also varies across the region). More sophisticated methods for distinguishing protocluster members (YSOs) from contaminants, as well as for conducting completeness corrections to account for sources missed in the bright nebosity, will be needed to place accurate constraints on the YSO surface density in the vicinity of G359.44a and to properly compare it with massive star formation models.

4.1.1. Outflows in the Main Sgr C Molecular Cloud

The outflow axes for G359.44a and G359.44b implied by the identified shocked emission features in this work correspond well with those identified using ALMA molecular line data in X. Lu et al. (2021). Figure 11 shows a comparison between the ALMA Band 6 SiO 5–4 line data and the NIRCcam data of outflows from each protostar.

The redshifted SiO emission from G359.44b, in particular, aligns very well with the line of outflow knots comprising knots 34, 32, and 27 (see Figure 7(b.1.3)), which extends for $\sim 5''$ (~ 0.2 pc). However, the blueshifted end of this source’s outflow is entirely invisible in the NIRCcam data, despite its prominence in SiO. This could be explained as the redshifted outflow from G359.44b entering into a region of much lower extinction than its blueshifted lobe, potentially in this case the outflow cavity cleared out by other sources in the region (e.g., G359.44a). This phenomenon, the redshifted outflow lobe being brighter than the blueshifted lobe, is well documented in other systems, such as the HH 80–81 system (J. Bally & B. Reipurth 2023, and references therein) and HH 135–136 system (see, e.g., Figures 1 and 5 of R. Fedriani et al. 2020), both of which host outflows with a significantly brighter redshifted lobe.

A similar process may be occurring with the bright chains of shocked H_2 emission just south of the main dark cloud, i.e., knots 17, 20, 23, 28, 29, 36, 16, 18, and 38 (see Figures 6(a) and 11). The brightness of these knots compared to material in the cloud could be explained by this material having just exited the high-extinction medium of the cloud, causing it to appear much brighter along our line of sight compared to the knots deep in the cloud. Some of these knots may be attributable to G359.44a and/or G359.44b; however, such an association is unclear, and they may have instead originated from other protostars in the cloud. Spatially coincident with the bright H_2 knots is what may be a bow shock in $\text{Br}\alpha$ (F405N) emission, labeled in Figure 11, which may have been driven by protostars in the cloud. Despite the brightness of this object, it may

instead be a fragment of the filamentary HII region, which dominates the F405N emission outside of the cloud (see the first panel of Figure 6).

The SiO emission measured by X. Lu et al. (2021) for G359.44a corresponds well with that seen in the infrared, particularly in encompassing knots 22 and 24. The blueshifted wide-angle outflow cone of G359.44a can also clearly be seen with NIRCcam (see, e.g., Figures 2 and 11), with knot 22 appearing to compose part of the outflow cavity wall close to the source and knot 24 composing part of the source’s jet, which flows through the middle of the wide-angle outflow cone (see Figure 7(b.1.3)). This is consistent with the understanding of jets and outflow cones in local, low-mass star-forming regions (see J. Bally 2016). The outflow cone detected in NIRCcam is also in good agreement with Spitzer IRAC2 $4.5 \mu\text{m}$ emission (shown as purple contours in Figure 11). This filter is known to trace both molecular hydrogen and CO emission from outflows from “extended green objects” (EGOs; C. J. Cyganowski et al. 2008; T. P. Ray et al. 2023), a class of objects of which G359.44a is a prominent example (X. Chen et al. 2013). From the NIRCcam data, we measure an opening angle of the outflow cone of G359.44a of $\sim 70^\circ$.

There are other outflow knots farther away that also appear to be associated with G359.44a: knots 19 (see Figure 7, panel (b.1.1)), 25 (panel (b.1.3)), 31 (panel (b.1.3)), 33 (panel (b.1)), 35 (panel (b.1)), and 37 (panel (b.1)). These knots trace out a curve that bends over its full extent, potentially indicating some precession of the protostar’s outflow axis over time. The chain of knots (from knot 37 to knot 19) is about $45''$ (or 1.75 pc at distance of 8.15 kpc) long. We can also make a rough estimation of the dynamical age for knot 37, which is likely the farthest knot associated with G359.44a. Assuming a knot velocity of $50\text{--}100 \text{ km s}^{-1}$ (see, e.g., R. Fedriani et al. 2018, 2020, for H_2 knot velocity estimations) and taking its angular separation ($\sim 36''$; see Table 4) at a distance of 8.15 kpc, we calculate a dynamical age of $\sim 14,000\text{--}28,000$ yr. This indicates that the G359.44a system is at least $\gtrsim 10^4$ yr old to have generated this object.

S. Kendrew et al. (2013) identified NIR emission in the vicinity of G359.44a and G359.44b in H_2 at $2.12 \mu\text{m}$ and in $\text{Br}\gamma$ ($2.16 \mu\text{m}$), which they proposed to represent shocked outflow material. Our data match well with the five line features identified in S. Kendrew et al. (2013) tracing their origin to G359.44a and G359.44b (see Figure 7(b.1.3)). In particular, the NIRCcam data would indicate that their features 1 and 2 correspond with emission from G359.44a, whereas features 3, 4, and 5 can be traced back to G359.44b.

Previous authors (e.g., S. Kendrew et al. 2013) found no evidence of star formation in the Sgr C cloud outside of the protostars G359.44a and G359.44b. The advances in sensitivity and spatial resolution brought by ALMA and JWST have revealed a population of dense submillimeter cores (X. Lu et al. 2020; A. V. I. Kinman et al. 2024) and widespread signs of outflow activity (X. Lu et al. 2021), indicating that the cloud is harboring significant star formation after all. We have identified ~ 40 line-emitting features that we associate with star formation activity in Sgr C besides G359.44a and G359.44b (see Table 4). Although there is a possibility that some of these objects could be shocked emission unrelated to star formation activity, or foreground to the CMZ and unrelated to Sgr C entirely, a survey of the line-emitting objects outside of star-forming regions in the data (presented in Appendix C) indicates

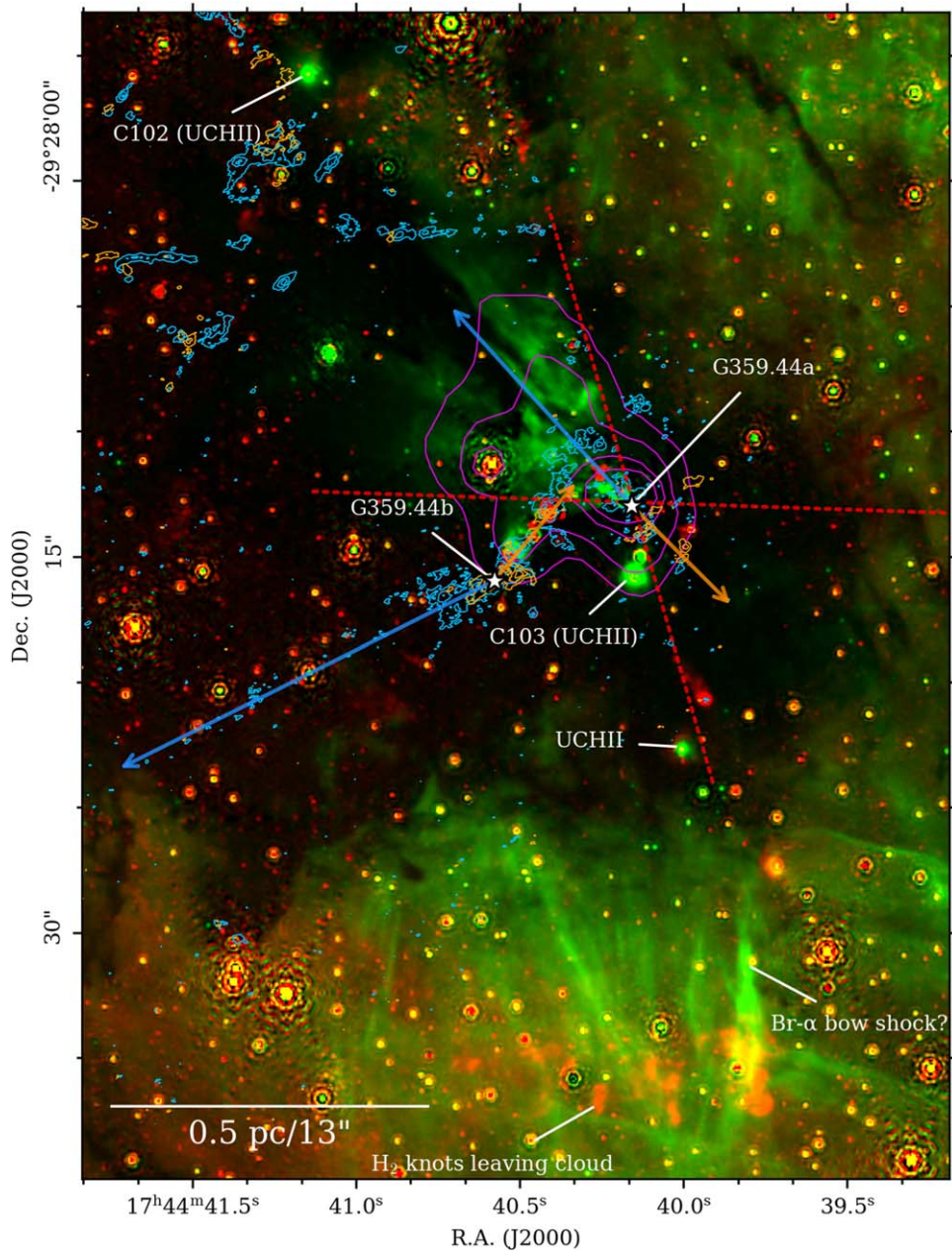


Figure 11. The region around G359.44a and G359.44b. F470N is shown in red and F405N in green, both continuum subtracted. The protostars are labeled and indicated by white stars. Blue and orange contours show ALMA Band 6 SiO 5–4 data from X. Lu et al. (2021) in blueshifted emission (integrated from -80 to -51 km s^{-1}) and redshifted emission (integrated from -48 to -25 km s^{-1}), respectively (similar to Figure 21 of X. Lu et al. 2021). Both sets of contours are shown with levels of 0.06, 0.12, and 0.18 Jy beam^{-1} , and pixels with primary beam response <0.6 have been masked. The blue- and redshifted outflow axis of each source is indicated by the blue and orange arrows, respectively. Purple contours show Spitzer IRAC2 $4.5 \mu\text{m}$ emission around G359.44a with levels of 50, 100, 200, and 300 MJy sr^{-1} . The outflow cone of G359.44a measured from the NIRCam data, with an opening angle of $\sim 70^\circ$, is indicated by the dotted red lines. Other features discussed in the text are labeled.

that there are relatively few, and those that are present are extended, dim, and clearly distinct from the concentrated knots of shocked H_2 emission associated with the main Sgr C cloud.

There is also the possibility that some of the identified knots could have been produced by large-scale shocks passing through Sgr C and interacting with its dense gas. However, it is noteworthy that many of these line-emitting features coincide with bright regions of ALMA Band 6 continuum data, which trace warm protostellar cores in the region (X. Lu et al. 2020); see, e.g., panels (b.1) and (b.2) of Figure 7. There is also a close correspondence between the features identified in F470N and the SiO 5–4 molecular line data presented in X. Lu et al.

(2021); this will be presented and discussed further in a forthcoming paper.

4.1.2. Comparison with JWST Studies of Massive Star Formation in the Galactic Disk

H. Beuther et al. (2023) present JWST MIRI-MRS spectro-imaging data on the massive star-forming complex IRAS 23385+6053 ($d \sim 5$ kpc), which acts as a useful Galactic disk counterpart to Sgr C. The MIRI data reveal a complicated system with multiple outflow structures, centered on the primary massive protostar ($m_* \sim 9 M_\odot$), in several MIR atomic

and molecular lines (H_2 , [Fe II], [Ne II]). These structures are corroborated by emission seen in 3.5 mm SiO 2–1 data taken with the IRAM Northern Extended Millimeter Array (NOEMA). Unlike IRAS 23385+6053, which displays at least three separate outflow axes centered at its main massive protostar in MIR 5.511 μm $\text{H}_2(0-0)\text{S}(7)$ emission (see Figure 5 of H. Beuther et al. 2023), Sgr C does not show evidence of multiple outflow axes for either of its main massive protostars, G359.44a and G359.44b, particularly in the MIR H_2 line filter F470N. Rather, single outflow axes for both G359.44a and G359.44b are well-defined in both IR and millimeter lines (see Figure 11), implying that they are forming relatively unperturbed by nearby YSOs, although G359.44a does demonstrate some indication of precession in its outflow that may have been caused by dynamical interactions with nearby sources (Section 4.1.1). This finding is somewhat counterintuitive, given the extremity of CMZ conditions compared to the Galactic disk; however, it may indicate that massive star formation can occur in the CMZ in a largely similar manner to that in the Galactic disk.

However, as the results of H. Beuther et al. (2023) indicate, multiple infrared tracers of jet/outflow emission, such as [Fe II] and [Ne II], which are not included in the present study, are needed to obtain a full picture of the different components of outflows in these regions. Additionally, measurements of accretion/ejection rates, the former of which H. Beuther et al. (2023) make with the Humphreys α H I(7–6) line at 12.37 μm , and probes of the warm/hot gas content (~ 200 – 2000 K) in the wider environment can place further constraint on massive star formation (C. Gieser et al. 2023). Therefore, high-resolution MIR spectroscopy measurements with JWST, on G359.44a/b and other CMZ massive protostars in other clouds (e.g., Sgr B, 50 km s^{-1} , 20 km s^{-1} , and the Brick; see A. Ginsburg et al. 2023, for more information about the Brick in particular), along with further studies on Galactic disk massive protostars (from, e.g., the IPA survey; T. Megeath et al. 2021; S. Federman et al. 2024), will be needed to construct a proper comparison between massive star formation in the CMZ and the Galactic disk.

4.1.3. Outflows in G359.42–0.104

Another promising result of analysis of the F470N continuum-subtracted emission near Sgr C is the discovery and tentative placement at the galactocentric distance of a new star-forming region, G359.42–0.104 (Section 3.5). The source G359.42a, the brightest infrared source in the region, may be a massive ($m_* > 8 M_\odot$) protostar, with a current stellar mass predicted by SED fitting of $m_* \simeq 9 M_\odot$ (Table 2). This claim is supported by its massive associated millimeter core ($M_{\text{mm}} \sim 90 M_\odot$) and the relatively large luminosity of its associated water maser, $\sim 1 \times 10^{-5} L_\odot$ (X. Lu et al. 2019b), which implies massive star formation activity as suggested by the relationship between H_2O maser luminosity and host source luminosity observed by J. S. Urquhart et al. (2011). It is worth noting, however, that the trend observed by J. S. Urquhart et al. (2011) experiences quite a substantial spread and that water masers are known to vary by orders of magnitude over relatively short timescales (X. Lu et al. 2019b). The lower bound on the current stellar mass of G359.42a, $m_* \simeq 3.5 M_\odot$, is also outside of the normal mass range for massive protostars ($m_* > 8 M_\odot$) and would instead be indicative of an intermediate-mass protostar. Additionally, the SED-fitting derived parameters and

measured millimeter core mass depend heavily on the adopted distance to the region, which we take to be at the galactocentric distance of 8.15 kpc, but which may be lower if the region is foreground to the CMZ. For example, if the distance to G359.42–0.104 is instead 4 kpc, the SED-fitting derived mass and millimeter core mass estimate would be $m_* \simeq 5 M_\odot$ and $M_{\text{mm}} \sim 22 M_\odot$, respectively.

A dynamical age estimate can be derived for G359.42a, as for G359.44a. Assuming a knot velocity of 50 – 100 km s^{-1} , and with an angular separation between the bright bow shock K21B and G359.42a of $\sim 26''$ and with our adopted distance to the source of 8.15 kpc, we estimate a dynamical age of $10,000$ – $20,000$ yr, placing a lower limit on the age of G359.42a of $\sim 10^4$ yr old, depending on its distance.

Although G359.42a is the only protostar in G359.42–0.104 associated with both a millimeter core and water maser, there is evidence for other protostars in the region. We call the most promising candidate G359.42b, which was identified based on the distinctive morphology of its surrounding emission (see Figure 8(c.2)). One of its associated emission-line objects, knot 13, has a morphology reminiscent of an outflow cone emanating from G359.42b; in this case, we estimate this outflow cone to have an opening angle of $\sim 40^\circ$. We also note that some of the outflow knots originating from G359.42b come in pairs on opposing sides of the source, e.g., knots 14 and 11 ($2''.31$ and $1''.97$ from G359.42b, respectively). This may provide an indication of episodic accretion resulting in the ejection of outflow knots from the source, a phenomenon that has been previously observed in massive star-forming regions (e.g., A. Caratti o Garatti et al. 2017; R. Cesaroni et al. 2018; R. Fedriani et al. 2023a). From end to end, the outflow from G359.44b appears to be $\sim 18''$ (~ 0.7 pc at a distance of 8.15 kpc), including knot 21A.

Ultimately, higher-sensitivity and higher-resolution observations of G359.42–0.104, especially in the millimeter and submillimeter, where individual protostellar cores can be identified and traced back to potential outflow knots, will be needed to disentangle the full picture of star formation in this region. Potential relationships with the Sgr C cloud, and especially with the Sgr C H II region, which is directly adjacent in projection to G359.42–0.104 (see Figure 6), may also be revealed with further observations and study of this star-forming region and its definitive placement at the CMZ distance (or not) with further data.

4.1.4. Outflows in the CMZ

The first unambiguous detection of protostellar outflows in the CMZ in the Sgr C cloud and their corroboration directly with ALMA, presented in this study, have significant implications for future infrared studies of the CMZ, especially in the infrared. Infrared observations of the CMZ, particularly those with the aim of resolving individual protostars and their associated outflow features, have been historically difficult for a number of reasons, most notably a lack of resolving power and the effects of extinction and crowding (F. Noguera-Lara et al. 2018, 2019). Studies that attempt to provide comprehensive identification and characterization of CMZ massive protostars (see, e.g., F. Yusef-Zadeh et al. 2009) have significant limitations in confirming protostellar detections and, in turn, constructing a robust catalog. For example, follow-up studies on the global sample of CMZ massive YSOs from F. Yusef-Zadeh et al. (2009) prove, using spectroscopic

follow-up, that many of the proposed detections are spurious and confused with cool late-type stars (see D. An et al. 2011; C. M. Koepferl et al. 2015; G. Nandakumar et al. 2018). The detection of outflows from candidate protostars in the infrared, finally possible with JWST, presents another robust way of differentiating between authentic protostars and contaminants using imaging alone.

Furthermore, individual infrared-luminous YSO counting is a key diagnostic for placing constraints on significant star formation parameters in the CMZ, such as the star formation rate and efficiency, which allows the CMZ to be appropriately compared and contrasted with regions in the main Galactic disk (J. D. Henshaw et al. 2023). In this respect, the ability of JWST NIRCcam to resolve individual knots of shocked emission comprising outflows from individual protostars is promising for future studies of CMZ star formation.

4.2. The Environment around Sgr C

Concerning the origins of star formation in Sgr C, recently evidence has also been put forward to suggest that Sgr C is undergoing triggered star formation. This is asserted on the basis of the “cometary” structure of the cloud, which points away from the Sgr C H II region, which contains many young, massive stars (F. Nogueras-Lara 2024), as well as the magnetic field orientations inferred from dust polarization measurements in this region, which appear to trace along the outline of the cloud, indicating an interface of interaction with the H II region (X. Lu et al. 2024; D. Paré et al. 2024). This proposition is also supported by the observed gradient of star formation occurring in the cloud, with the most massive star formation (e.g., G359.44a and G359.44b) occurring closest (in projection) to the interface between the H II region and the cloud where the compression on the cloud (and therefore its density) would be highest, and with the lower-mass star formation tapering off going away from the H II region and deeper into the cloud.

Ionized gas has been revealed in great detail in the NIRCcam observations via the F405N filter ($\text{Br}\alpha$; see Figure 1). This H II region hosts prominent filamentary striations that are also seen in longer-wavelength observations of other CMZ H II regions, i.e., those associated with Sgr B2 and Sgr B1 (e.g., 1.28 GHz MeerKAT observations presented in I. Heywood et al. 2022). These filaments are intriguing. Their linear morphologies indicate a potential role for strong magnetic fields in controlling the structure of the nebula. However, the wide variety of position angles of the features, including near-orthogonal orientations at similar sky positions, indicates a potentially complicated 3D structure that we are viewing in projection. High-resolution spectra of recombination lines associated with these structures will be helpful to better understand the dynamics of this ionized gas. A further analysis and discussion of these $\text{Br}\alpha$ filaments and their potential formation mechanism will be presented in a forthcoming paper.

5. Conclusions

In this paper, we have presented NIRCcam observations of the CMZ star-forming region Sgr C that, along with ancillary IR and millimeter data, provide a high level of detail into the star formation activity of the main cloud and its surroundings. We have characterized the two most massive protostars in the heart of the main Sgr C protocluster, G359.44a and G359.44b, and obtained their physical properties via SED fitting; in

particular, masses of $\sim 20 M_{\odot}$ have been derived for each protostar. We have made a cross-match between JWST sources and ALMA cores in order to identify a sample of lower-mass protostars. From these sources, there are five matches that are redder than the overall population, which we take to be our strongest sample of low-mass YSOs in the cloud. We have carried out a census of the narrowband NIRCcam data, using the filters F212N, F405N, and F470N, which trace shocked molecular and atomic hydrogen emission from protostellar jets, to identify line-emitting features. We have identified 88 features, which we believe to comprise protostellar outflows from over a dozen protostellar outflows in the NIRCcam data. We attribute about a quarter of these outflow knots to the massive protostars G359.44a and G359.44b, forming an outflow axis for each protostar that agrees well with molecular line data from ALMA and archival IR data from Spitzer. There are ~ 40 others likely originating from other, lower-mass star formation activity in the cloud.

The remaining outflow knots are attributed to a newly discovered star-forming region, G359.42–0.104, located $\sim 1'$ to the south of the main Sgr C protocluster. NIRCcam data in G359.42–0.104 reveal a pair of prominent bow shocks in both F470N and F212N (tracing H_2 shocked emission), which we estimate to have originated from two protostars, G359.42a and G359.42b, the former of which we speculate may be a massive protostar owing to its SED-fitted inferred mass ($m_* > 8 M_{\odot}$). However, the distance to this region, as well as whether it is inside the CMZ or foreground, is still uncertain.

Acknowledgments

This work is based on observations made with the NASA/ESA/CSA JWST and Hubble Space Telescope. The data were obtained from the Mikulski Archive for Space Telescopes at the Space Telescope Science Institute, which is operated by the Association of Universities for Research in Astronomy, Inc., under NASA contract NAS 5-03127 for JWST. These observations are associated with program 4147. Support for program 4147 was provided by NASA through a grant from the Space Telescope Science Institute, which is operated by the Association of Universities for Research in Astronomy, Inc., under NASA contract NAS 5-03127. This paper makes use of the following ALMA data: ADS/JAO.ALMA 2016.1.00243.S, ADS/JAO.ALMA 2021.1.00172.L. ALMA is a partnership of ESO (representing its member states), NSF (USA) and NINS (Japan), together with NRC (Canada), NSTC and ASIAA (Taiwan), and KASI (Republic of Korea), in cooperation with the Republic of Chile. The Joint ALMA Observatory is operated by ESO, AUI/NRAO and NAOJ. The National Radio Astronomy Observatory and Green Bank Observatory are facilities of the National Science Foundation operated under cooperative agreement by Associated Universities, Inc.

The authors thank the anonymous referee for constructive comments. The authors would like to acknowledge X. Lu for providing access to the reduced ALMA Band 6 continuum and molecular data and for fruitful discussions. The authors would like to acknowledge M. Reid for insightful discussion and clarification. S.T.C. acknowledges support from the award JWST-GO-04147.003-A. R.F. acknowledges support from the grants Juan de la Cierva FJC2021-046802-I, PID2020-114461GB-I00, and PID2023-146295NB-I00. R.F., L.B.F., and R.S. acknowledge financial support from the Severo Ochoa grant CEX2021-001131-S funded by MCIN/AEI/ 10.13039/

501100011033. Additionally, L.B.F. and R.S. acknowledge support from grant EUR2022-134031 funded by MCIN/AEI/10.13039/501100011033 and by the European Union Next-GenerationEU/PRTR and grant PID2022-136640NB-C21 funded by MCIN/AEI 10.13039/501100011033 and by the European Union. Y.Z. acknowledges the support from the Yangyang Development Fund. Y.C. was partially supported by a Grant-in-Aid for Scientific Research (KAKENHI No. JP24K17103) of the JSPS. J.B. acknowledges support by the National Science Foundation through grant No. AST-1910393. A.G. acknowledges support from the NSF under grants AAG

2008101, 2206511, and CAREER 2142300. Y.-L.Y. acknowledges support from Grant-in-Aid from the Ministry of Education, Culture, Sports, Science, and Technology of Japan (20H05845, 20H05844) and a pioneering project in RIKEN (Evolution of Matter in the Universe). Z.-Y.L. is supported in part by NSF AST- 2307199 and NASA 80NSSC20K0533.

Appendix A Photometry Used for SED Fitting

Table [A1](#) shows the integrated flux densities for all filters used for SED fitting in Section [3.2](#).

Table A1
Integrated Flux Densities

Name	$F_{1.15}$	$F_{1.62}$	$F_{1.82}$	$F_{3.6}$ (NIRCam)	$F_{3.6}$ (Spitzer)	$F_{4.5}$	$F_{4.8}$	$F_{5.6}$	$F_{8.0}$	$F_{25.2}$	$F_{37.1}$	F_{70}	F_{160}	F_{250}	F_{350}	F_{500}
	(Jy)	(Jy)	(Jy)	(Jy)	(Jy)	(Jy)	(Jy)	(Jy)	(Jy)	(Jy)	(Jy)	(Jy)	(Jy)	(Jy)	(Jy)	(Jy)
G359.44a	...	0.0032	0.0040	0.022	0.018	0.12	0.15	0.23	0.21	14.3	43.1	340.1	380.9	90.1	17.7	2.1
	...	(0.0017)	(0.0023)	(0.011)	(0.022)	(0.05)	(0.05)	(0.06)	(0.02)	(1.5)	(4.5)	(34.1)	(217.1)	(109.9)	(47.0)	(13.4)
G359.44b	...	0.0024	0.0035	0.015	0.019	0.035	0.040	0.038	0.0035	2.21	14.7	113.5	127.0	30.0	5.89	0.70
	...	(0.0006)	(0.0018)	(0.005)	(0.014)	(0.040)	(0.044)	(0.046)	(0.0128)	(1.11)	(3.9)	(11.4)	(72.4)	(36.6)	(15.67)	(4.48)
G359.42a	0.00010	0.00068	0.0014	...	0.11	0.28	...	0.54	0.72	3.9	4.2	2.4	0.51	0.11	0.014	0.0062
	(0.00076)	(0.0018)	(0.0022)	...	(0.012)	(0.03)	...	(0.056)	(0.08)	(0.49)	(0.1)	(0.1)	(18.69)	(7.90)	(3.041)	(0.9873)

Note. Filters in which a flux was not measured for a source, because it was either invisible or saturated, are marked with ellipses. $F_{1.15}$, $F_{1.62}$, $F_{1.82}$, $F_{3.6}$ (first appearance), and $F_{4.8}$ refer to JWST NIRCam data at 1.15, 1.62, 1.82, 3.60, and 4.80 μm , respectively. $F_{3.6}$ (second appearance), $F_{4.5}$, $F_{5.6}$, and $F_{8.0}$ refer to Spitzer IRAC data at 3.6, 4.5, 5.6, and 8.0 μm , respectively. $F_{25.2}$ and $F_{37.1}$ refer to SOFIA-FORCAST data at 25.2 and 37.1 μm , respectively. F_{70} , F_{160} , F_{250} , F_{350} , and F_{500} refer to Herschel PACS/SPIRE data at 70, 160, 250, 350, and 500 μm , respectively. The second row for each source refers to the error associated with the flux at each wavelength.

Appendix B Knot Feature Significance Level Maps

Figures B1, B2, and B3 present magnified views of all knot features identified in F470N, F212N, and F405N, respectively. Only the first panel of figure B1 and figure B2 is shown in the text; the remaining panels are available as figure sets.

R.A.=17:44:37.99 Dec.=-29:29:20.92

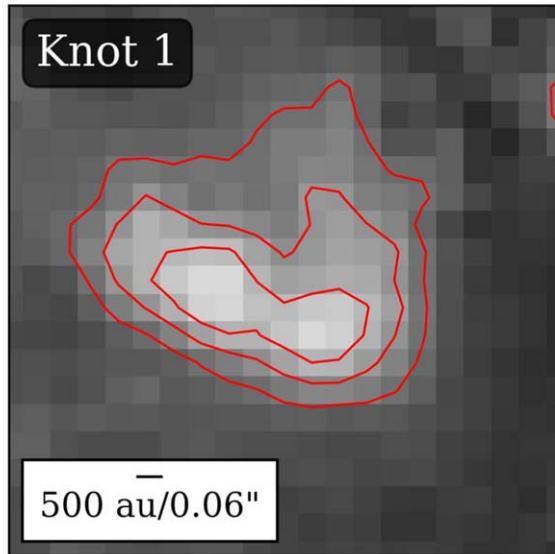


Figure B1. Significance level contour maps of all knot features identified in the F470N continuum-subtracted image and compiled in Table 4. The central coordinates of each knot determined from the peak pixel are given on the top of each panel. A physical scale bar of 500 au is given in the lower left corner of each panel; north is up and east is to the left in all panels.

(The complete figure set (80 images) is available in the [online article](#).)

R.A.=17:44:38.12 Dec.=-29:29:13.73

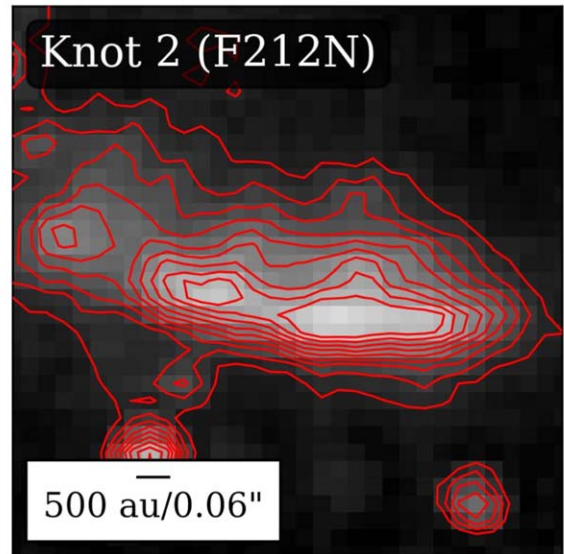


Figure B2. Significance level contour maps of all knot features identified in the F212N continuum-subtracted image and compiled in Table 4. The central coordinates of each knot determined from the peak pixel are given on the top of each panel. A physical scale bar of 500 au is given in the lower left corner of each panel; north is up and east is to the left in all panels.

(The complete figure set (22 images) is available in the [online article](#).)

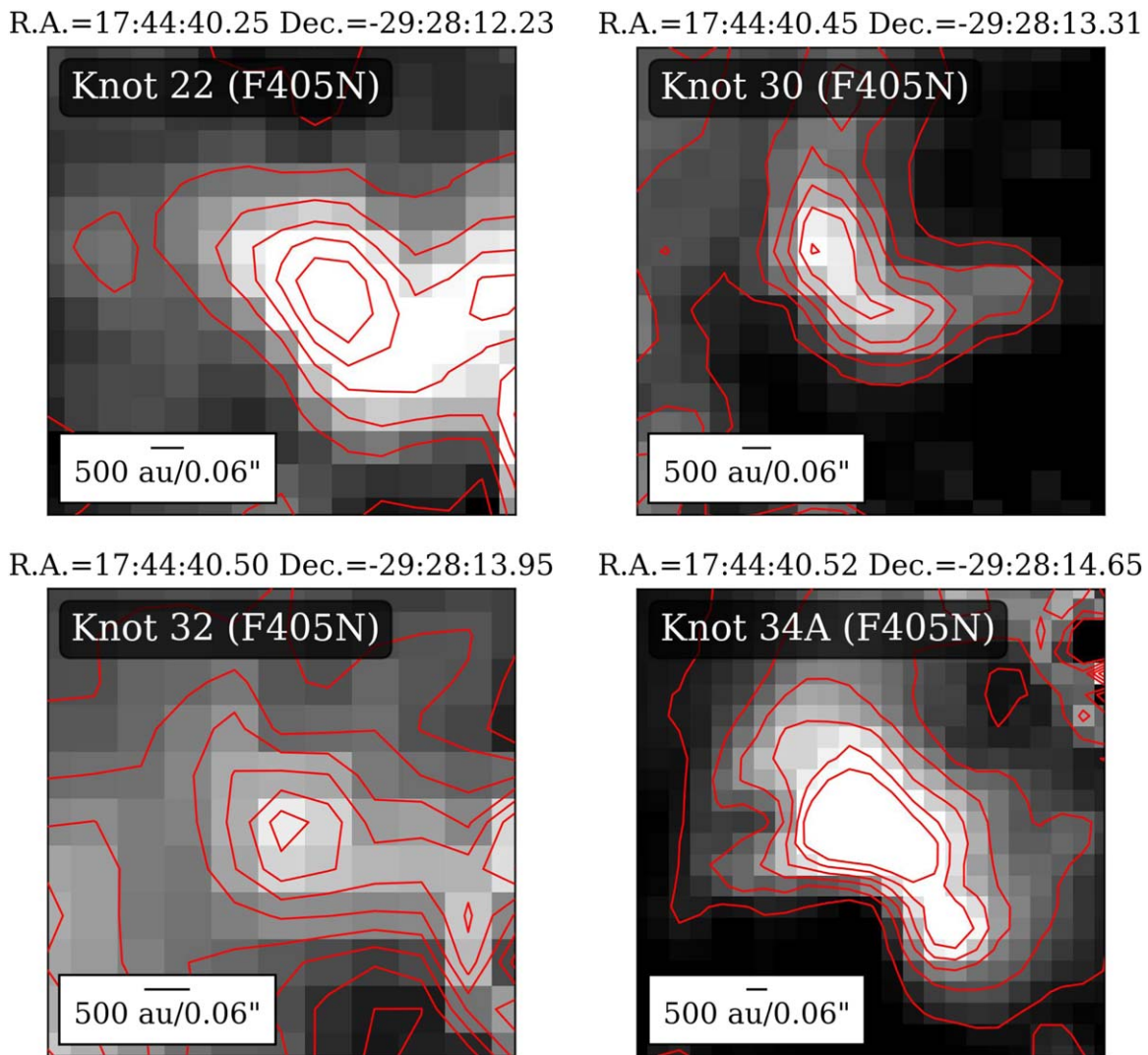


Figure B3. Significance level contour maps of all knot features identified in the F405N continuum-subtracted image and compiled in Table 4. The contour levels shown for knots 22 and 34A represent 25σ to 300σ in steps of 55σ above the local background; those shown for knots 30 and 32 represent 20σ to 300σ in steps of 20σ . The central coordinates of each knot determined from the peak pixel are given on the top of each panel. A physical scale bar of 500 au is given in the lower left corner of each panel; north is up and east is to the left in all panels.

Appendix C Miscellaneous MHOs in the NIRCam Field

In addition to the outflow knot candidates associated with star formation activity, a number of miscellaneous MHOs were also discovered in the NIRCam field. These are compiled in Table C1 and briefly shown and described here.

C.1. The Lobes

The Lobes are two relatively bright extended sources of emission to the far southeast of the NIRCam pointing. Their symmetric nature may indicate a bipolar outflow from a young star.

C.2. Filaments and the Flame

The Flame is another prominent object located in the southwest corner of the NIRCam image, close to G359.42 -0.104 and associated with a dark cloud. Notably, this structure is surrounded by filaments in the H_2 emission, the origins of which are unclear. Similar filaments can be seen in the eastern part of the Sgr C cloud (see Figure 6(b.2)). This region may host star formation, but it is notably lacking any associated emission in ALMA Band 3, VLA (X. Lu et al. 2019a), and MeerKAT (I. Heywood et al. 2022) images.

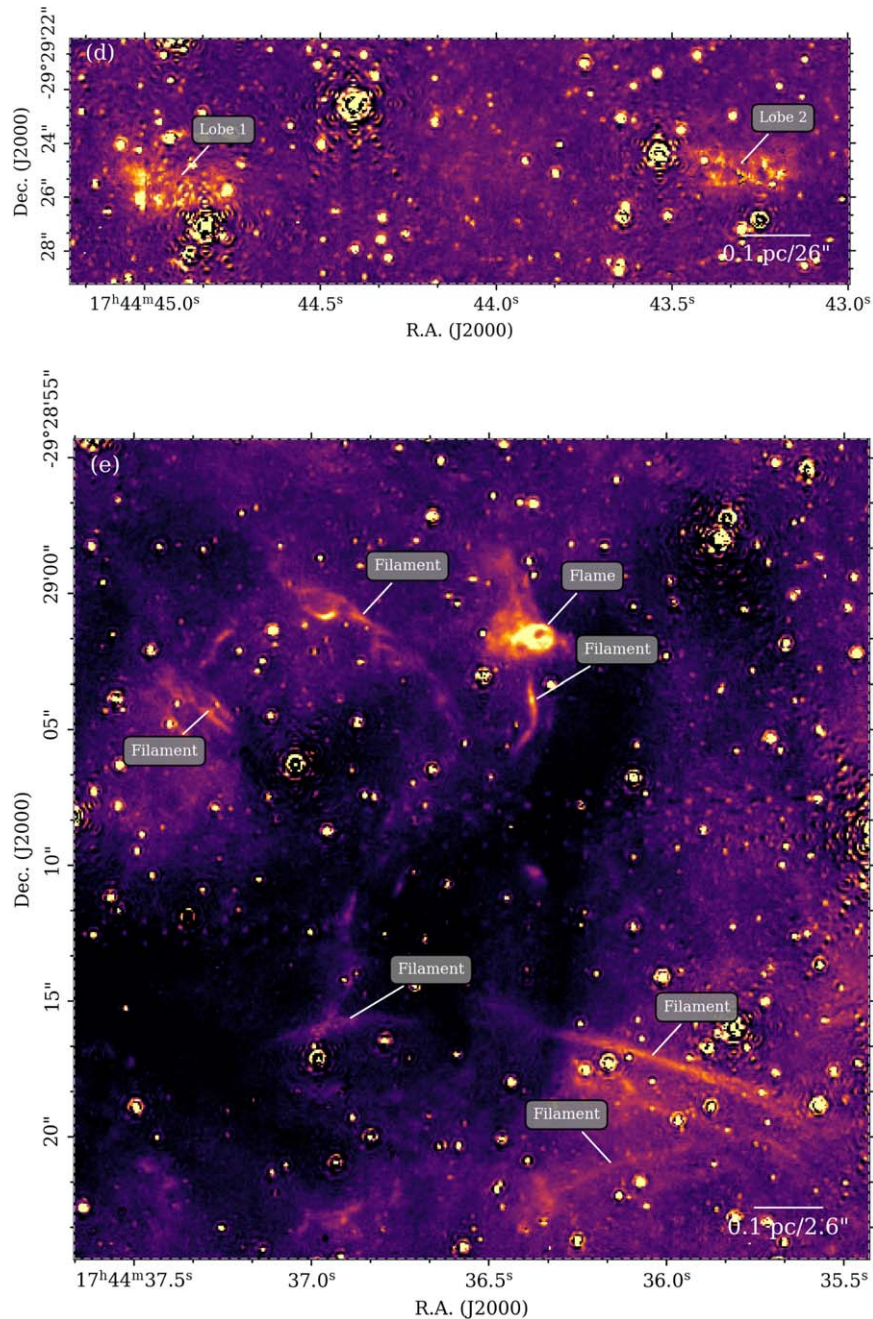


Figure C1. Compilation of miscellaneous MHOs found in the continuum-subtracted F470N NIRCam data.

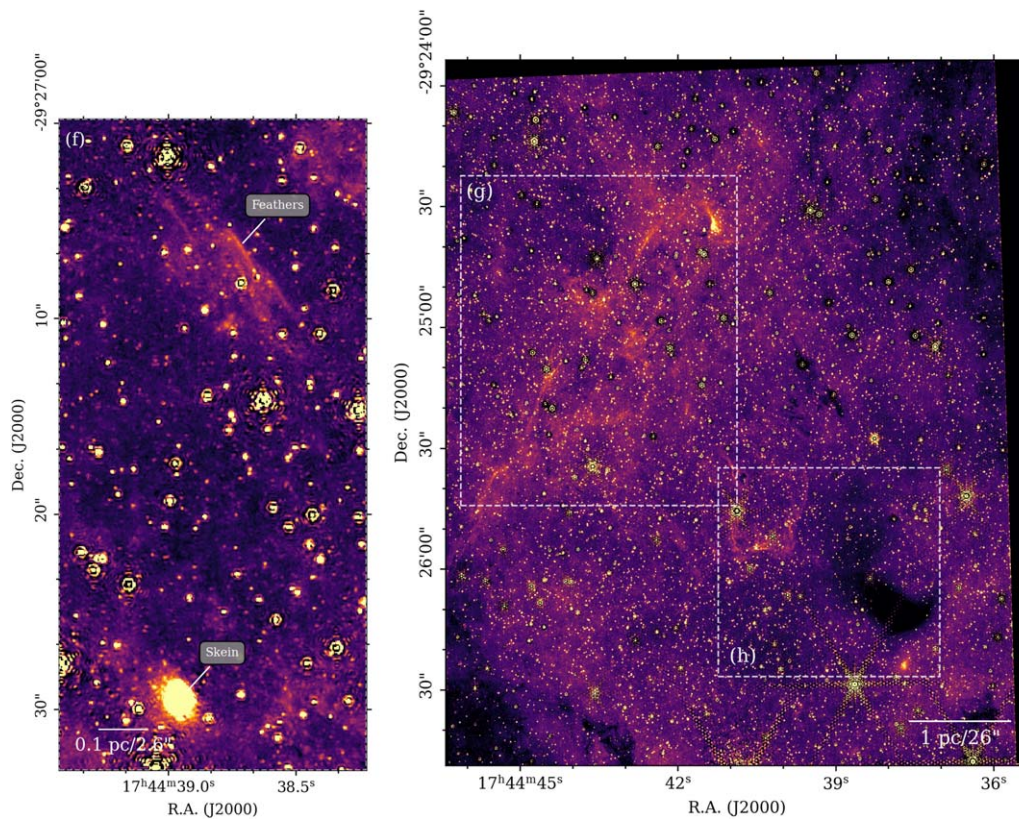


Figure C1. (Continued.)

C.3. The Skein and the Feathers

The Skein is a notable bright region of extended emission in the NIRCcam data; this object is also visible in Spitzer and SOFIA MIR images of the CMZ, indicating that it is not an artifact of the NIRCcam data (e.g., a “snowball”¹⁵). One may speculate that this object is a background galaxy or a YSO, but its origin is nonetheless unknown.

The Feathers are another filamentary feature, similar to the filaments seen around the Flame.

C.4. The Streak

The Streak is a very bright region of extended emission prominently visible in the JWST continuum images of Sgr C (see Figure 1), as well as in the F470N continuum-subtracted data.

While the origin and nature of this object are uncertain, it is spatially coincident with a type II Cepheid star (b333_57_97584) detected in V. F. Braga et al. (2019), as well as a tentative YSO candidate (SSTGC 368854) reported in

D. An et al. (2011) that is negated by Spitzer IRS spectroscopic follow-up. The NIRCcam data do not provide any further clarity into the origin of this object.

C.5. The Threads and the Lamp

The Threads (numbered 1–6) are filamentary structures seen in the NIRCcam data, which appear to extend for as much as a parsec in length (if at the distance to the CMZ; angular size $\sim 25''$). These filaments also appear similar in structure to those seen in the main Sgr C cloud (labeled in Figure 6(b.2)) and around the Flame (Figure C1). Although such H_2 filaments are likely of different origin than the HI filaments seen in $Br\alpha$ (F405N) in the Sgr C HII region, it is possible that the two share a similar formation mechanism.

The Lamp is another bright emission feature, origin otherwise unknown, located in projection adjacent to a prominent dark cloud.

¹⁵ <https://jwst-docs.stsci.edu/depreciated-jdox-articles/data-artifacts-and-features/snowballs-and-shower-artifacts>

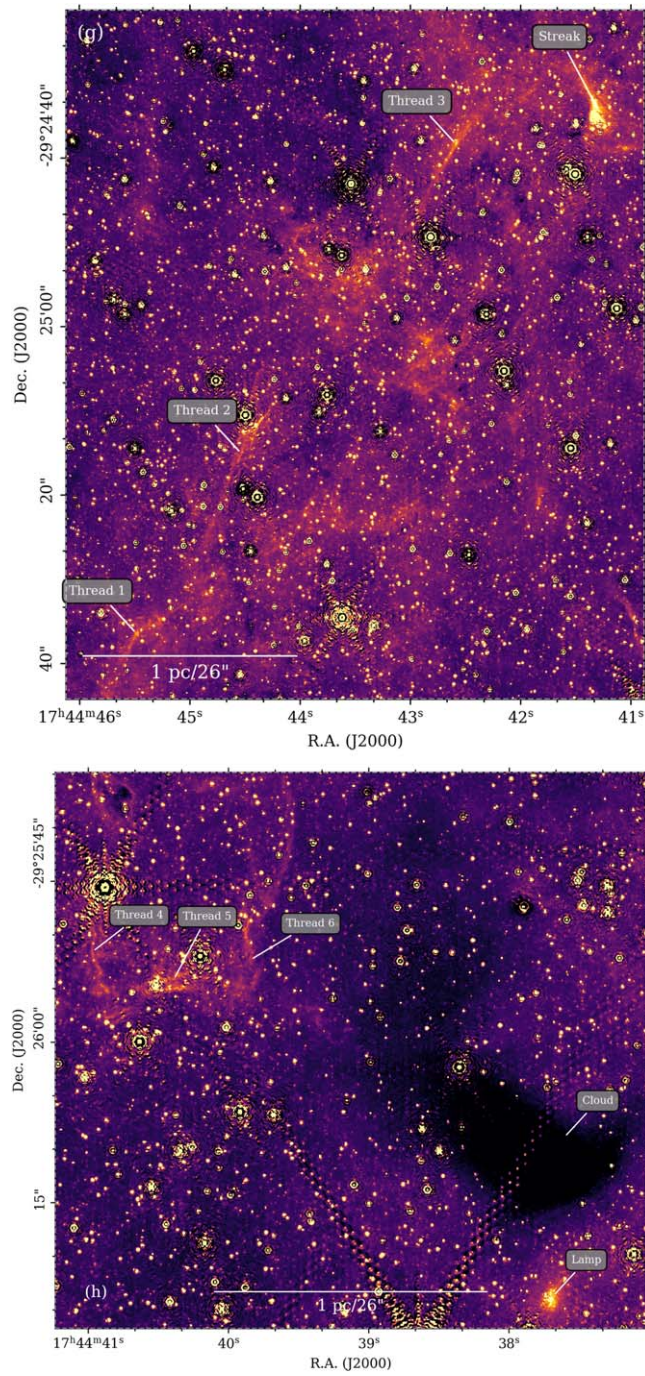


Figure C1. (Continued.)





Table C1

Miscellaneous Molecular Hydrogen Objects Found in the F470N Continuum-subtracted NIRCcam Image

Name	R.A. (J2000)	Decl. (J2000)
Lobe 1	17:44:44.91	-29:29:25.56
Lobe 2	17:44:43.31	-29:29:24.91
Flame	17:44:36.37	-29:29:01.57
Skein	17:44:38.96	-29:27:29.38
Feathers	17:44:38.75	-29:27:06.61
Thread 1	17:44:45.52	-29:25:37.42
Thread 2	17:44:44.54	-29:25:15.12
Thread 3	17:44:42.63	-29:24:39.08
Thread 4	17:44:40.95	-29:25:52.61
Thread 5	17:44:40.37	-29:25:54.31
Thread 6	17:44:39.86	-29:25:50.67
Streak	17:44:41.33	-29:24:33.82
Lamp	17:44:37.71	-29:26:24.00

Note. Approximately central coordinates for each feature are given.

ORCID iDs

Samuel Crowe  <https://orcid.org/0009-0005-0394-3754>
 Rubén Fedriani  <https://orcid.org/0000-0003-4040-4934>
 Jonathan C. Tan  <https://orcid.org/0000-0002-3389-9142>
 Alva Kinman  <https://orcid.org/0009-0008-6570-9287>
 Yichen Zhang  <https://orcid.org/0000-0001-7511-0034>
 Morten Andersen  <https://orcid.org/0000-0002-5306-4089>
 Lucía Bravo Ferres  <https://orcid.org/0009-0004-4390-7937>
 Francisco Noguerras-Lara  <https://orcid.org/0000-0002-6379-7593>
 Rainer Schödel  <https://orcid.org/0000-0001-5404-797X>
 John Bally  <https://orcid.org/0000-0001-8135-6612>
 Adam Ginsburg  <https://orcid.org/0000-0001-6431-9633>
 Yu Cheng  <https://orcid.org/0000-0002-8691-4588>
 Yao-Lun Yang  <https://orcid.org/0000-0001-8227-2816>
 Sarah Kendrew  <https://orcid.org/0000-0002-7612-0469>
 Chi-Yan Law  <https://orcid.org/0000-0003-1964-970X>
 Joseph Armstrong  <https://orcid.org/0000-0002-4855-1325>
 Zhi-Yun Li  <https://orcid.org/0000-0002-7402-6487>

References

- An, D., Ramírez, S. V., Sellgren, K., et al. 2011, *ApJ*, 736, 133
 Bally, J. 2016, *ARA&A*, 54, 491
 Bally, J., & Reipurth, B. 2023, *ApJ*, 958, 99
 Beroiz, M., Cabral, J. B., & Sanchez, B. 2020, *A&C*, 32, 100384
 Beuther, H., van Dishoeck, E. F., Tychoniec, L., et al. 2023, *A&A*, 673, A121
 Bonnell, I. A., Bate, M. R., Clarke, C. J., & Pringle, J. E. 2001, *MNRAS*, 323, 785
 Braga, V. F., Contreras Ramos, R., Minniti, D., et al. 2019, *A&A*, 625, A151
 Brasseur, C. E., Rogers, T., Donaldson, T., et al. 2020, in ASP Conf. Ser. 522, *Astronomical Data Analysis Software and Systems XXVII*, ed. P. Ballester et al. (San Francisco, CA: ASP), 97
 Breen, S. L., Ellingsen, S. P., Contreras, Y., et al. 2013, *MNRAS*, 435, 524
 Bushouse, H., Eisenhamer, J., Dencheva, N., et al. 2023, JWST Calibration Pipeline, v1.12.5, Zenodo, doi:10.5281/zenodo.10022973
 Caratti o Garatti, A., Stecklum, B., Garcia Lopez, R., et al. 2017, *NatPh*, 13, 276
 Caratti o Garatti, A., Stecklum, B., Weigelt, G., et al. 2016, *A&A*, 589, L4
 Carey, S. J., Noriega-Crespo, A., Mizuno, D. R., et al. 2009, *PASP*, 121, 76
 Carlson, E., Linden, T., & Profumo, S. 2016, *PhRvD*, 94, 063504
 Caswell, J. L., Fuller, G. A., Green, J. A., et al. 2010, *MNRAS*, 404, 1029
 Cesaroni, R., Moscadelli, L., Neri, R., et al. 2018, *A&A*, 612, A103
 Chen, X., Gan, C.-G., Ellingsen, S. P., et al. 2013, *ApJS*, 206, 9
 Cotton, W. D., & Yusef-Zadeh, F. 2016, *ApJS*, 227, 10
 Crocker, R. M., Jones, D. I., Melia, F., Ott, J., & Protheroe, R. J. 2010, *Natur*, 463, 65
 Crowe, S., Fedriani, R., Tan, J. C., et al. 2024, *A&A*, 682, A2
 Cyganowski, C. J., Whitney, B. A., Holden, E., et al. 2008, *AJ*, 136, 2391
 De Buizer, J. M., Liu, M., Tan, J. C., et al. 2017, *ApJ*, 843, 33
 Diolaiti, E., Bendinelli, O., Bonaccini, D., et al. 2000, *A&AS*, 147, 335
 Federman, S., Megeath, S. T., Rubinstein, A. E., et al. 2024, *ApJ*, 966, 41
 Fedriani, R., Caratti o Garatti, A., Cesaroni, R., et al. 2023a, *A&A*, 676, A107
 Fedriani, R., Caratti o Garatti, A., Coffey, D., et al. 2018, *A&A*, 616, A126
 Fedriani, R., Caratti o Garatti, A., Koutoulaki, M., et al. 2020, *A&A*, 633, A128
 Fedriani, R., Tan, J. C., Telkamp, Z., et al. 2023b, *ApJ*, 942, 7
 Ferrière, K., Gillard, W., & Jean, P. 2007, *A&A*, 467, 611
 Gaia Collaboration, Vallenari, A., Brown, A. G. A., et al. 2023, *A&A*, 674, A1
 Gieser, C., Beuther, H., van Dishoeck, E. F., et al. 2023, *A&A*, 679, A108
 Ginsburg, A., Bally, J., Barnes, A. T., et al. 2024, *ApJL*, 968, L11
 Ginsburg, A., Barnes, A. T., Battersby, C. D., et al. 2023, *ApJ*, 959, 36
 Ginsburg, A., Henkel, C., Ao, Y., et al. 2016, *A&A*, 586, A50
 Ginsburg, A., Sipőcz, B. M., Brasseur, C. E., et al. 2019, *AJ*, 157, 98
 Givone, U., Sternberg, A., Lutz, D., Feuchtgruber, H., & Pauldrach, A. W. A. 2002, *ApJ*, 566, 880
 Gregg, B., Calzetti, D., Adamo, A., et al. 2024, *ApJ*, 971, 115
 Grudić, M. Y., Guszejnov, D., Offner, S. S. R., et al. 2022, *MNRAS*, 512, 216
 Hankins, M. J., Lau, R. M., Radomski, J. T., et al. 2020, *ApJ*, 894, 55
 Henshaw, J. D., Barnes, A. T., Battersby, C., et al. 2023, in ASP Conf. Ser. 534, *Protostars and Planets VII*, ed. S. Inutsuka et al. (San Francisco, CA: ASP), 83
 Heywood, I., Rammala, I., Camilo, F., et al. 2022, *ApJ*, 925, 165
 Kendrew, S., Ginsburg, A., Johnston, K., et al. 2013, *ApJL*, 775, L50
 Kinman, A. V. I., Petkova, M. A., Tan, J. C., Cosentino, G., & Cheng, Y. 2024, arXiv:2403.04032
 Koepferl, C. M., Robitaille, T. P., Morales, E. F. E., & Johnston, K. G. 2015, *ApJ*, 799, 53
 Kruijssen, J. M. D., Dale, J. E., & Longmore, S. N. 2015, *MNRAS*, 447, 1059
 Law, C., & Yusef-Zadeh, F. 2004, *ApJ*, 611, 858
 Liu, M., Tan, J. C., De Buizer, J. M., et al. 2019, *ApJ*, 874, 16
 Liu, M., Tan, J. C., De Buizer, J. M., et al. 2020, *ApJ*, 904, 75
 Long, K. S., Blair, W. P., Winkler, P. F., & Lacey, C. K. 2020, *ApJ*, 899, 14
 Lu, X., Cheng, Y., Ginsburg, A., et al. 2020, *ApJL*, 894, L14
 Lu, X., Li, G.-X., Zhang, Q., & Lin, Y. 2022, *NatAs*, 6, 837
 Lu, X., Li, S., Ginsburg, A., et al. 2021, *ApJ*, 909, 177
 Lu, X., Liu, J., Pillai, T., et al. 2024, *ApJ*, 962, 39
 Lu, X., Mills, E. A. C., Ginsburg, A., et al. 2019a, *ApJS*, 244, 35
 Lu, X., Zhang, Q., Kauffmann, J., et al. 2016, in IAU Symp. 322, *The Multi-Messenger Astrophysics of the Galactic Centre* (Cambridge: Cambridge Univ. Press), 99
 Lu, X., Zhang, Q., Kauffmann, J., et al. 2019b, *ApJ*, 872, 171
 McKee, C. F., & Tan, J. C. 2003, *ApJ*, 585, 850
 Megeath, T., Anglada, G., Atmagulov, P., et al. 2021, JWST Proposal. Cycle, 1, #1802
 Molinari, S., Bally, J., Noriega-Crespo, A., et al. 2011, *ApJL*, 735, L33
 Molinari, S., Schisano, E., Elia, D., et al. 2016, *A&A*, 591, A149
 Morris, M., & Serabyn, E. 1996, *ARA&A*, 34, 645
 Muzerolle, J., Hartmann, L., & Calvet, N. 1998, *AJ*, 116, 2965
 Nandakumar, G., Schultheis, M., Feldmeier-Krause, A., et al. 2018, *A&A*, 609, A109
 Noguerras-Lara, F. 2022, *A&A*, 666, A72
 Noguerras-Lara, F. 2024, *A&A*, 681, L21
 Noguerras-Lara, F., Gallego-Calvente, A. T., Dong, H., et al. 2018, *A&A*, 610, A83
 Noguerras-Lara, F., Schödel, R., Gallego-Calvente, A. T., et al. 2019, *A&A*, 631, A20
 Noguerras-Lara, F., Schödel, R., & Neumayer, N. 2021, *A&A*, 653, A33
 Noguerras-Lara, F., Schödel, R., & Neumayer, N. 2022, *NatAs*, 6, 1178
 Nonhebel, M., Barnes, A. T., Immer, K., et al. 2024, *A&A*, 691, A70
 Ossenkopf, V., & Henning, T. 1994, *A&A*, 291, 943
 Paré, D., Butterfield, N. O., Chuss, D. T., et al. 2024, *ApJ*, 969, 150
 Pillai, T., Kauffmann, J., Tan, J. C., et al. 2015, *ApJ*, 799, 74
 Ray, T. P., McCaughrean, M. J., Caratti o Garatti, A., et al. 2023, *Natur*, 622, 48
 Reid, M. J., Menten, K. M., Brunthaler, A., et al. 2019, *ApJ*, 885, 131
 Reiter, M., Morse, J. A., Smith, N., et al. 2022, *MNRAS*, 517, 5382
 Rieke, M. J., Kelly, D., & Horner, S. 2005, *Proc. SPIE*, 5904, 1
 Rosen, A. L., Offner, S. S. R., Sadavoy, S. I., et al. 2020, *SSRv*, 216, 62
 Rosolowsky, E. W., Pineda, J. E., Kauffmann, J., & Goodman, A. A. 2008, *ApJ*, 679, 1338

- Schödel, R., Noguera-Lara, F., Gallego-Cano, E., et al. 2020, *A&A*, **641**, A102
- Schultheis, M., Fritz, T. K., Nandakumar, G., et al. 2021, *A&A*, **650**, A191
- Simpson, J. P. 2018, *ApJ*, **857**, 59
- Sormani, M. C., Treß, R. G., Ridley, M., et al. 2018, *MNRAS*, **475**, 2383
- Stolovy, S., Ramirez, S., Arendt, R. G., et al. 2006, *JPhCS*, **54**, 176
- Tan, J. C., Beltrán, M. T., Caselli, P., et al. 2014, in *Protostars and Planets VI*, ed. H. Beuther et al. (Tucson, AZ: Univ. of Arizona Press), 149
- Urquhart, J. S., Morgan, L. K., Figura, C. C., et al. 2011, *MNRAS*, **418**, 1689
- Wang, P., Li, Z.-Y., Abel, T., & Nakamura, F. 2010, *ApJ*, **709**, 27
- Young, C. H., & Evans, N. J., II 2005, *ApJ*, **627**, 293
- Yusef-Zadeh, F., Hewitt, J. W., Arendt, R. G., et al. 2009, *ApJ*, **702**, 178
- Yusef-Zadeh, F., Morris, M., & Chance, D. 1984, *Natur*, **310**, 557
- Zhang, Y., & Tan, J. C. 2018, *ApJ*, **853**, 18